Surface winds off Peru-Chile: Observing closer to the coast from radar altimetry

O. Astudillo [a,b,*], B. Dewitte [a,b,f,g], M. Mallet [c], F. Frappart [b,d], J.A. Rutllant [a,e], M. Ramos [a,f,g,h], L. Bravo [f,g], K. Goubanova [a,f,i], S. Illig [b,j]

[a] Centro de Estudios Avanzados en Zonas Áridas (CEAZA), La Serena, Chile
[b] Laboratoire d'Etudes en Géophysique et Océanographie Spatiale (LEGOS), Toulouse, France
[c] CNRM UMR 3589, Météo-France/CNRS, Toulouse, France
[d] Géosciences Environnement Toulouse (GET), Toulouse, France
[e] Departamento de Geofísica, Facultad de Ciencias Físicas y Matemáticas, Universidad de Chile, Santiago, Chile
[f] Departamento de Biología Marina, Facultad de Ciencias del Mar, Universidad Católica del Norte, Coquimbo, Chile
[g] Millennium Nucleus for Ecology and Sustainable Management of Oceanic Islands (ESMOI), Coquimbo, Chile
[h] Centro de Innovación Acuícola Aquapacifico, Universidad Católica del Norte, Coquimbo, Chile
[i] CECI UMR 5318 - CNRS/CERFACS, Toulouse, France
[j] Departament of Oceanography, MARE Institute, University of Cape Town, South Africa

ARTICLE INFO

ABSTRACT

The near-shore surface mesoscale atmospheric circulation in the upwelling systems off Peru and Chile is influential on the Sea Surface Temperature through Ekman transport and pumping. There has been a debate whether or not the so-called "wind drop-off", that is a shoreward decrease of the surface wind speed near the coast, can act as an effective forcing of upwelling through Ekman pumping. Although the wind drop-off has been simulated by high-resolution atmospheric models, it has not been well documented due to uncertainties in the scatterometry-derived wind estimates associated with land contamination. Here we use the along-track altimetry-derived surface wind speed data from ENVISAT, Jason-1, Jason-2, and SARAL satellites, to document the spatial variability of the mean wind drop-off near the coast as estimated from the inversion of the radar backscattering coefficient. The data are first calibrated so as to fit with the scatterometer observations of previous and current satellite missions (QuikSCAT, ASCAT). The calibrated data are then analyzed near the coast and a wind drop-off scale is estimated. The results indicate that the wind drop-off takes place all along the coast, though with a significant alongshore variability in its magnitude. Differences between products are shown to be related both to the differences in repeat cycle between the different altimetry missions and to the peculiarities of the coastline shape at the coastal latitudes of the incident tracks. The relative contribution of Ekman pumping and Ekman transport to the total transport is also estimated indicating a comparable contribution off Chile while transport associated to Ekman pumping is on average ~1.4 larger than Ekman transport off Peru. Despite the aliasing effect associated with the weak repetitivity of the satellite orbit and the high frequency variability of the winds in this region, the analysis suggests that the seasonal cycle of the surface winds near the coast could be resolved at least off Peru.

© 2017 Elsevier Inc. All rights reserved.

1. Introduction

Eastern Boundary Current Systems (EBUS) have drawn interest in recent years due to the societal concern on the possible changes that the rich marine ecosystems they host could experience under the influence of anthropogenic climate forcing (Bakun et al., 2015; Wang et al., 2015a). A main driver of the oceanic circulation in these regions is the along-shore momentum flux that promotes upwelling of nutrient-rich waters through Ekman dynamics. While the locally wind-forced processes that generate upwelling are well known and consist in two mechanisms, i.e. Ekman pumping and Ekman transport (Sverdrup et al., 1942) most studies of upwelling systems have focused on the investigation of Ekman transport (i.e., along-shore wind stress) and its relationship to various aspects of the regional oceanic circulation (Sea Surface Temperature (SST), productivity, fisheries) (Carr and Kearns, 2003; Chavez and Messié, 2009; Demarcq, 2009; Wang et al., 2015b; among many others). The relative contribution of both processes has in fact remained ubiquitous due to limitations of the satellite

* Corresponding author at: Centro de Estudios Avanzados en Zonas Áridas (CEAZA), La Serena, Chile.
  E-mail address: orlando.astudillo@gmail.com (O. Astudillo).

scatterometer measurements (ERS, QuikSCAT), which contain a 28 to 50-km wide blind zone along the coast limiting the description of the mesoscale atmospheric circulation within this narrow coastal fringe. The relatively low spatial resolution of these products has also resulted in uncertainty in the actual magnitude of the wind stress curl near the coast (Croquette et al., 2007). Despite recent improvements in the space resolution of the global atmospheric reanalysis products, the uncertainty in the wind stress curl estimations in the coastal band has persisted due to model biases (Wood et al., 2011) and to the scarcity of in situ observations to constrain data assimilation. This has resulted in a significant dispersion within the available products of the mean surface winds. To illustrate the latter statement, Fig. 1 presents the alongshore horizontal wind profiles at three major upwelling cells along the coast of Peru and Chile from satellite observations (QuikSCAT/ASCAT, Jason-1), the atmospheric reanalysis ERA-Interim (Dee et al., 2011) produced by the European Centre for Medium-Range Weather Forecasts (ECMWF) and the National Centers for Environmental Prediction (NCEP) Climate Forecast System Reanalysis (CFSR, Saha et al., 2010). First, it is readily apparent that reanalysis products cannot resolve the coastal zone due to their low resolution; and second, they do not agree in the magnitude and cross-shore variability of the winds in the first 200 km off the coast. In addition, regional modeling studies suggest that the wind stress near the coast in EBUS experiences a shoreward decrease in amplitude, the so-called wind drop-off, that results in a wind stress curl favorable to Ekman pumping (Capet et al., 2004; Renault et al., 2012). Observational evidence of such drop-off has been elusive due to the sparse data in the coastal fringe, although field experiments do suggest its existence in some regions, in particular off central Chile (e.g., Garreaud et al., 2011; Bravo et al., 2015).

The uncertainties resulting from the extrapolation of scatterometer winds in near-coastal regions for forcing high-resolution oceanic

models have also been a limitation for gaining confidence in model results (Renault et al., 2012). Indeed, in most EBUS regional modeling studies, gridded QuikSCAT surface wind estimates have been used, implying that wind data have been extrapolated on the ocean model grid from, at best, 28 km offshore to the closest coastal grid point of the ocean model. In the process, there is the possibility that compensating effects exist between the Ekman transport and Ekman pumping on SST (e.g., a weaker (stronger) than observed drop-off would lead to a stronger (weaker) Ekman transport near the coast). Interestingly in regional simulations of upwelling systems, a mean cold bias is usually diagnosed (Penven, 2005; Penven et al., 2001; Veitch et al., 2009; Machu et al., 2009) which could reflect a bias in the balance between Ekman pumping and transport, although such a bias could be also attributed to a warm bias in some satellite based SST datasets (Dufois et al., 2012).

Moreover, coupled physical-biogeochemical coastal processes show a great sensitivity to near shore wind stress curl in upwelling regions (Albert et al., 2010) and the ecosystem dynamics is also likely critically dependent on the coastal wind pattern through its effects on mesoscale activity (Renault et al., 2016).

Therefore, there is a real need to improve our knowledge in the mesoscale atmospheric circulation in coastal regions given the need for a realistic simulation of the oceanic circulation for downstreamed applications (e.g. directed toward resources management). This is particularly true for the Peru-Chile EBUS, known as the Humboldt Current System (HCS), which hosts the most productive marine ecosystem in the world (Chavez et al., 2008). Upwelling off Chile and Peru drive an exceptionally high biological productivity (Carr and Kearns, 2003) due to the persistent equatorward low-level alongshore flow that maintains a coastal band of nutrient-rich cold waters extending from about 40°S to the equator (Hill et al., 1998; Silva et al., 2009). Measurements of surface winds over the HCS are sparse in space and time, lacking systematic,
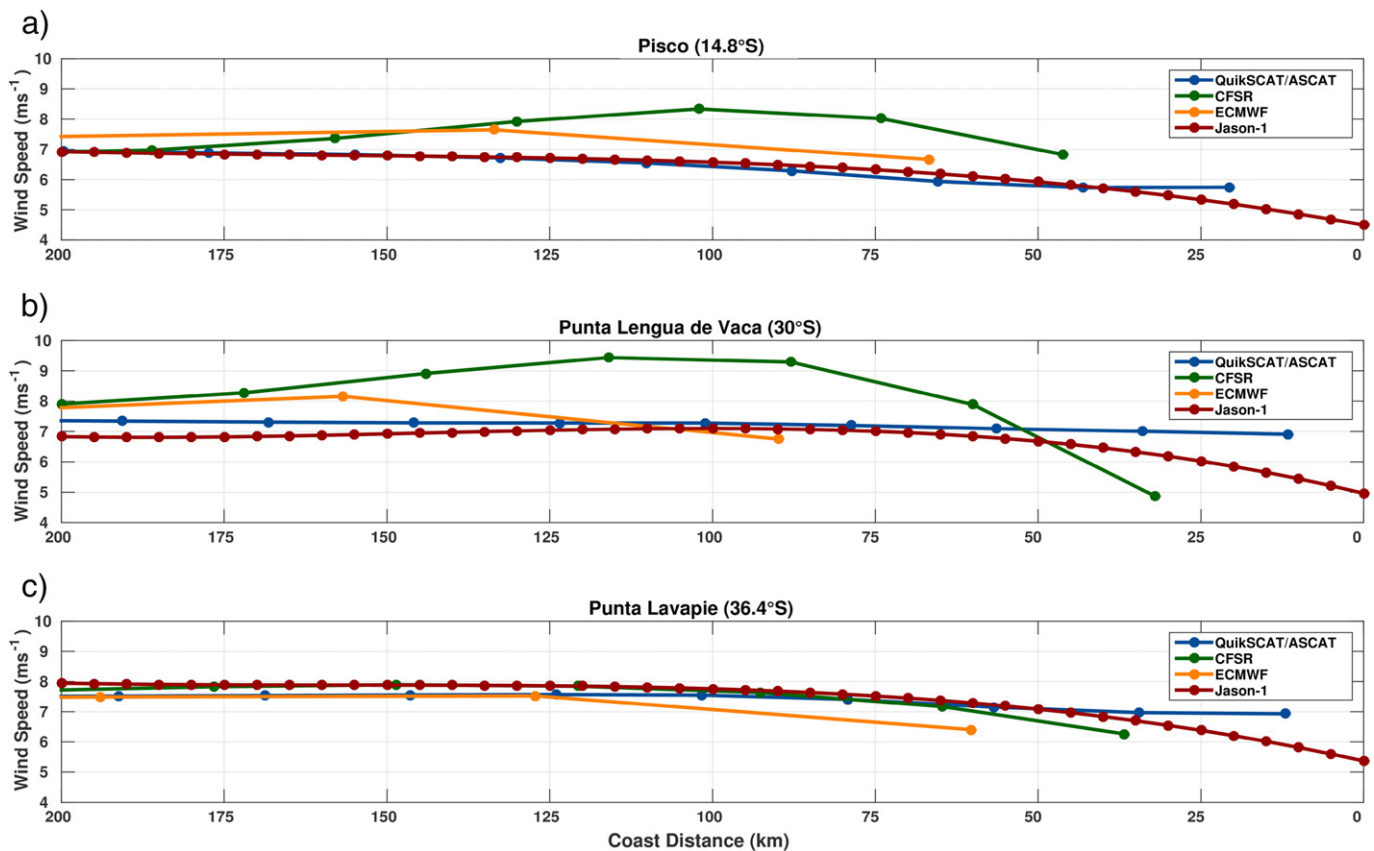

Fig. 1. Zonal mean cross-shore 10-m wind speed at (a) Pisco (14.8°S), (b) Punta Lengua de Vaca (30°S) and (c) Punta Lavapie (36.4°S) over the period 2000–2010. The blue, red, green, and orange lines are for QuikSCAT-ASCAT (0.25° horizontal resolution) scatterometers, Jason-1 (0.045°) altimeter, the CFSR (0.3°) and ERA-Interim (0.75°) reanalyses respectively. (For interpretation of the references to colour in this figure legend, the reader is referred to the web version of this article.)

dense, and long-term monitoring of the near shore area. Most studies analyzing the upwelling favorable winds off Chile and Peru have relied on satellite-borne scatterometer data (Figueroa and Moffat, 2000; Halpern, 2002; Garreaud and Muñoz, 2005; Muñoz, 2008; Renault et al., 2009; Albert et al., 2010; Dewitte et al., 2011; Aguirre et al., 2012) or atmospheric reanalysis and regional models (Renault et al., 2012; Rahn and Garreaud, 2013, Bravo et al., 2015) and have focused on regional features (e.g., large scale coastal jets) rather than on coastal mesoscale circulation.

Here we take advantage of altimeter-derived surface wind speeds from four different altimeter missions (ENVISAT, Jason-1, Jason-2 and SARAL) to assess the near-shore surface atmospheric circulation. The surface wind speeds are retrieved using the backscattering coefficient at Ku-band (Ka-band for SARAL). The focus here is on the mean coastal winds due to inherent limitations of the satellites missions for addressing synoptic-scale variability that is prominent in the region of interest (see Section 2).

The paper is organized as follow: Section 2 provides a detailed description of the satellite sensors and the datasets employed. Section 3 describes the methods used for the altimeter data calibration examining their consistency against winds measured by the scatterometers. In Section 4 mean altimeter-derived coastal winds are analyzed focusing on the intensity and alongshore variability of the wind drop-off, and on estimating the relative contributions of Ekman transport and pumping. Concluding remarks and a discussion are presented in Section 5.

2. Data sources

2.1. Satellite altimetry data

Wind speeds derived from Radar Altimeters (RA) sensors at the Ku-band (13.575 GHz) onboard ENVISAT, Jason-1, Jason-2 and Ka-band (35.75 GHz) onboard SARAL are used in this study. A RA is a nadir-looking active microwave device that measures with high accuracy the time delay, the power and the shape of the reflected radar pulses for determining the satellite height with respect to the earth surface. Radar echo parameters can also be used to derive the significant wave height (SWH) and the surface wind speed (U_{10}) (Lefèvre et al., 2006; Queffeulou et al., 1999).

Surface wind speeds are empirically estimated by their effect on the intensity of the return pulse of the radar echo (i.e., backscattering coefficient (σ_0)). With increasing wind speed the sea surface becomes rougher so that the number of specularly reflecting faces decreases and more energy is scattered back in off-nadir directions. This leads to a decrease in the intensity of the mean backscattered power, which can thus be related to the surface wind speed (Ikeda and Dobson, 1995). In order to increase the confidence of the altimeter-derived geophysical parameters, the return pulses are typically averaged over time to provide one data point every second along the satellite ground track. With a satellite ground scanning velocity of 5.8 km^{-1} for Jason-1/Jason-2 and 7.45 km^{-1} for ENVISAT/SARAL each altimeter data value represents an elongated area (footprint) ranging between 1 and 10 km in diameter according to the range, pulse width and SWH (Chelton et al., 1989/2001; Zieger et al., 2009). The small altimeter footprint allows resolving the 50-km fringe along the coast, thus surpassing the scatterometer capabilities subject to retrieval errors onshore due to their large footprint (Yang et al., 2011). On the other hand, unlike scatterometers RA instruments allow deriving only the wind speed because there is no significant dependence of σ_0 on wind direction at small incidence angles.

2.1.1. Jason-1 & 2

These missions were launched on December 7th 2001 and June 20th, 2008. Jason-1 is a cooperative programme between the French Space Agency (Centre National d'Etudes Spatiales, CNES) and the U.S. National

Aeronautics and Space Administration (NASA) while Jason-2 is a cooperation among CNES, NASA, the European Meteorological Satellite Organization (EUMETSAT) and the U.S. National Oceanic and Atmospheric Administration (NOAA), respectively. Their main payload is the Poseidon-2(3) radar altimeter from CNES, the Jason/Advanced Microwave Radiometer (JMR/AMR) from JPL/NASA, and a triple system for precise orbit determination: the real-time tracking system DIODE of DORIS instrument from CNES, a GNSS receiver and a Laser Retroflector Array (LRA) from NASA. They orbit at an altitude of 1336 km, with an inclination of 6°, on a 10-day repeat cycle, providing observations of the Earth surface (ocean and land) from 66° South to North, with an equatorial ground-track spacing of about 315 km. Topex/Poseidon formerly used this orbit. Poseidon-2 and Poseidon-3 radar altimeters are dual-frequency solid-state altimeters that measure accurately the distance between the satellite and the surface (range) and provide ionospheric corrections over the ocean. They operate at Ku (13.575 GHz) and C (5.3 GHz) bands. Raw data are processed by SSALTO (Segment Sol multimissions d'ALTimétrie, d'Orbitographie). Jason-1 was decommissioned in July 2013.

2.1.2. ENVISAT (ENVironmental SATellite)

This mission was launched on March 1st 2002 by the European Space Agency (ESA). It carries 10 instruments including the advanced radar altimeter (RA-2). It is based on the heritage of the sensor onboard the European Remote Sensing (ERS-1 and 2) satellites. RA-2 was a nadir-looking pulse-limited radar altimeter operating at Ku- (13.575 GHz), as ERS-1 and 2, and S- (3.2 GHz) bands. Its goal was to collect radar altimetry data over ocean, land and ice caps. ENVISAT orbits at an average altitude of 790 km, with an inclination of 98.54°, on a sun-synchronous orbit with a 35-day repeat cycle. It provided observations of the Earth surface (ocean and land) from 82.4° latitude South to 82.4° latitude North. This orbit was formerly used by ERS-1 and 2 missions, with an equatorial ground-track spacing of about 85 km. ENVISAT remained on its nominal orbit until October 2010 and its mission ended on April 8th 2012.

2.1.3. SARAL (Satellite with Argos and ALtika)

This joint French-Indian mission between the CNES and the Indian Space Research Organization (ISRO) was launched on February 25th 2013. Its payload is composed of the AltiKa radar altimeter, a dual-frequency radiometer and a triple system for precise orbit determination: the real-time tracking system DIODE of DORIS instrument, a Laser Retroflector Array (LRA), and the Advanced Research and Global Observation Satellite (ARGOS-3). Its initial orbital characteristics were the same as for ENVISAT (see above). The first four cycles of SARAL did not follow precisely the ENVISAT orbit. AltiKa radar altimeter is a solid-state mono-frequency altimeter that provides accurate range measurements. It is the first and the only altimeter to operate at the Ka-band (35.75 GHz).

Data used in this study are the along-track values of U_{10} made available along with corresponding track and cycle numbers, acquisition time, latitude, longitude and the distance to the coast from the Geophysical Data Records (GDRs) of the different altimetry missions. These data come from GDR T patch 2 for SARAL, GDR v2.1 for ENVISAT, GDR C for Jason-1 and GDR D for Jason-2. They are available at the Centre de Topographie de l'Océan et de l'Hydrosphère (CTOH – http://ctoh.legos.obs-mip.fr/).

The wind speed is estimated through the inversion of a relationship with the Ku-band backscatter coefficient (corrected for atmospheric attenuation) and the significant wave height using a neural network for Jason-1 and Jason-2 (Gourrion et al., 2002). For ENVISAT, the empirical model used to retrieve the wind speed is given by (Abdalla, 2012):

$$U_{10} = U_m + 1.4U_m^{0.096}e^{-0.32U_m^{1.096}} \qquad (1)$$

With $U_m = \begin{cases} \alpha - \beta\sigma_0^a & \text{if } \sigma_0^a \leq \sigma_0^{\lim} \\ \gamma e^{-\delta\sigma_0^a} & \text{if } \sigma_0^a > \sigma_0^{\lim} \end{cases}$ $\qquad (2)$
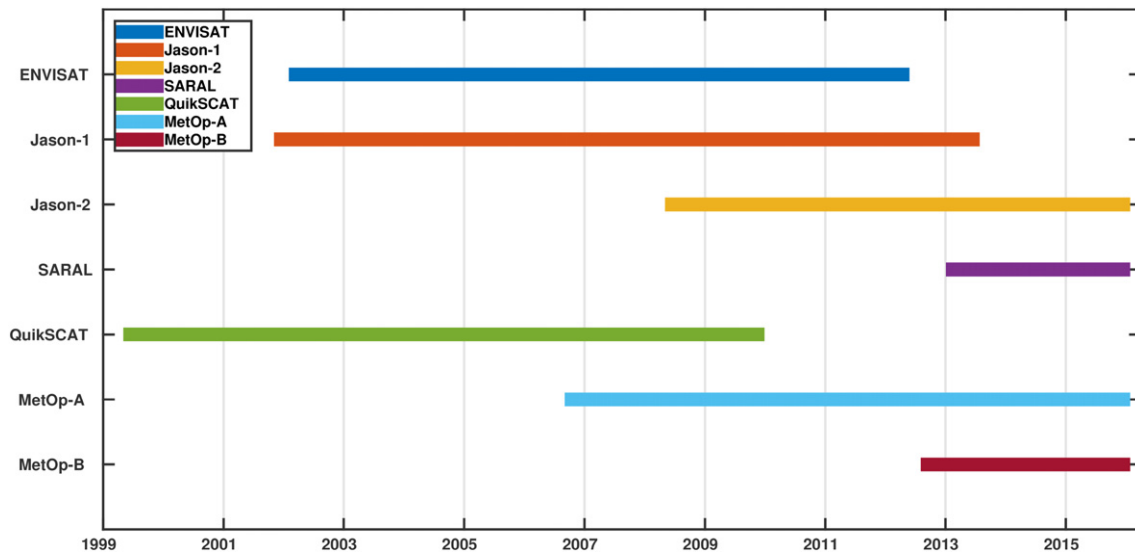
Fig. 2. Temporal coverage of the satellite missions.

where U_m is a first-guess estimation of U_{10} while $\alpha = 46.5$, $\beta = 3.6$, $\gamma = 1690$, $\delta = 0.5$, $\sigma_0^{\lim} = 10.917$ dB are the fitting parameters. For SARAL, the same formulation as for ENVISAT is used with the following fitting parameters values $\alpha = 34.2$, $\beta = 2.48$, $\gamma = 711.6$, $\delta = 0.42$, $\sigma_0^{\lim} = 11.409$ dB (Lillibridge et al., 2014).

Details on the time periods and technical specifications (e.g., repeat cycle, inclination, and footprint) for each satellite mission are provided in Fig. 2 and Table 1.

2.2. Satellite scatterometer data

Wind scatterometry is a widely used technique that measures wind speeds and directions over the ocean surface. The measurement principle differs from the altimeters because it is based on the Bragg resonant scattering mechanism, for which backscatter power is directly proportional to the distribution and density of capillary and short gravity waves on the sea surface (Queffeulou et al., 1999).

This study uses the scatterometer Sea Winds aboard the QuikSCAT satellite and the Advanced SCATterometer (ASCAT) aboard Metop-A and Metop-B satellites. QuikSCAT was a mission that lasted from June 1999 to November 2009; meanwhile the ongoing series of Metop-A and Metop-B satellites were launched on October 2006 and September 2012 respectively. We used two types of scatterometer products:

1. Level-2: The L2-swath products provide wind vector retrievals at 12.5-km sampling resolution on a non-uniform grid within the swath, with 12-hour repeat cycles between the ascending and descending satellite passes, enabling their utilization for the altimeter validation and calibration. Here we used the new reprocessed datasets (QuikSCAT, ASCAT) optimized for coastal ocean (Fore et al., 2014; KNMI, 2010, 2013; SeaPAC, 2013).

2. Level-3: The L3-gridded products contain wind vector fields corresponding to the daily average of both L2-swath passes interpolated onto a regular grid of 0.25° in longitude and latitude using objective method. We used the new daily-averaged gridded wind fields (QuikSCAT, ASCAT) to validate the calibrated altimeters winds (Bentamy and Fillon, 2012).

The accuracy of scatterometer products was determined in several studies using moored buoys, in which the RMS differences did not exceed 2 ms^{-1} and 20° for wind speed and direction, respectively at global scale (Bentamy et al., 2008; Vogelzang et al., 2011; Verhoef and Stoffelen, 2013).

3. Methods

3.1. Calibration of the altimeter data

3.1.1. Quality control

A three-pass quality-control process was applied to the data. Firstly, we have rejected from the analysis all quality-flagged data and all measurements identified as over land. Secondly, if $U_{10} < 1$ ms^{-1}, then the data point was flagged as erroneous due to the significant biases related to damping of Bragg waves at very low wind speeds (Yang et al., 2011). Finally, if $U_{10} > 20$ ms^{-1}, then the data point was discarded because the

Table 1
Summary of the main technical characteristics by satellite mission. The effective footprint size for the altimeters is related to SWH = 5 m (Chelton et al., 1989, 2001; Zieger et al., 2009; Callahan and Lungu, 2006; Verhoef and Stoffelen, 2013; Verron et al., 2015; http://www.aviso.altimetry.fr/missions).

Satellite	Operation period	Repetitivity	Inclination	Altitude	Instrument	Frequency	Footprint	Format	Agency
ENVISAT	March 2002–April 2012	35 days (cycle)	98.54°	790 km	Radar Altimeter-2	Ku band (13.575 GHz)	~5.6 × 15 km	Alongtrack	ESA
Jason-1	December 2001–June 2013	10 days (cycle)	66.04°	1336 km	POSEIDON-2	Ku band (13.575 GHz)	~6.9 × 20 km	Alongtrack	NASA,CNES
Jason-2	June 2008–present	10 days (cycle)	66.04°	1336 km	POSEIDON-3	Ku band (13.575 GHz)	~6.9 × 20 km	Alongtrack	NASA, CNES, NOAA, EUMESAT
SARAL	February 2013–present	35 days (cycle)	98.55°	790 km	AltiKa	Ka band (35.75 GHz)	~5.6 × 8 km	Alongtrack	ISRO,CNES
QuikSCAT	June 1999–November 2009	12 h (pass)	98.61°	802.4 km	SeaWinds	Ku band (13.4 GHz)	~25 × 37 km	Swath Gridded	NASA
Metop-A	October 2006–present	12 hour (pass)	98.7°	817 km	ASCAT-A	C band (5.255 GHz)	~10 × 20 km	Swath Gridded	ESA, EUMETSAT
Metop-B	September 2012–present				ASCAT-B				

wind vector algorithms for QuikSCAT are developed for the wind speeds less than this limit (Quilfen et al., 2007).

3.1.2. Validation

The wind speeds derived from the altimeters were matched against the L2-swath (12.5-km) and L3-gridded (28-km) scatterometer products considered here as the "reference" source data. The comparison between the altimeter and scatterometer data was carried out over a domain that excludes the 50-km width coastal band and extends offshore for 250 km. The outliers that had a wind speed difference between paired altimeter and scatterometer greater than three standard deviations were excluded from the analysis. The sequential procedure was performed in three steps:

1. We matched all the valid altimeter values by mission with the L2-swath scatterometer data. A collocation criteria was chosen in order to get statistically significant number of comparison from both ascending/descending scatterometer passes in the minimum space/time limits, i.e. 12.5 km in space and 60 min for Jason-1/Jason-2 and 120–240 min for ENVISAT/SARAL. The temporal relaxation for ENVISAT/SARAL is necessary given the limited time span of their overpass over the study region.
2. The daily averages (reference time 12:00) from the L3-gridded data were interpolated to the altimeter tracks locations using a natural neighbor interpolation scheme (Shanas et al., 2014) producing a daily temporal match-up.
3. Statistics describing the comparisons were conducted characterizing the differences between the altimeters and both scatterometer products including conventional, linear moments and the regression parameters.

Table 2 summarizes the statistics of the validation of the altimeter data against the reference products over the selected time periods (i.e., ENVISAT: Jan. 2003–Dec. 2009; SARAL: Mar. 2013–Apr. 2014; Jason-1: Jan. 2002–Dec. 2008; Jason-2: Jan. 2009–Dec. 2013). Additionally we provide the statistics classified into three categories of low (<4 ms^{-1}), medium (4–10 ms^{-1}) and high (>10 ms^{-1}) wind speeds.

The first collocated datasets (i.e., altimeter versus L2-swath) were limited in number (62,110/30,375 hits of the total available for ENVISAT/SARAL and 19,748/13,262 for Jason-1/Jason-2, respectively) due to the stringent time/space collocation criteria and to the reduced time periods of the morning (descending passes) and the evening (ascending passes) orbit segments from the L2-swath scatterometer. The frequency distribution of the altimeter/scatterometer by wind speed category corresponds on average to ~20%, ~72% and ~8% for low, medium and high winds respectively. The outliers account for ~5% of the paired values for ENVISAT/SARAL and ~8% for Jason-1/Jason-2. The overall Pearson's correlation coefficients (ρ) are high for all satellites (above 0.95) and the wind speed differences are characterized by a rather small mean bias of ~-0.5 ms^{-1}, Root-Mean-Square Error (RMSE) of ~0.9 ms^{-1} and Mean Absolute Error (MAE) of ~0.8 ms^{-1}. The highest discrepancies were found for low winds in ENVISAT and Jason-1 (see Table 2).

The second collocated dataset (i.e., altimeter versus L3-gridded) amounts to ~95% of the valid altimeter values. The frequency distribution presents similar percentages for wind categories as for the L2-swath data. The agreement in statistics between altimeter and scatterometer decreases unsurprisingly as a function of the temporal gridding of the reference products (i.e. daily averages in L3-gridded versus instantaneous values for L2-swath) consistent with Monaldo (1988). The mean correlation coefficients, bias, RMSE and MAE are ~0.9, ~-0.4 ms^{-1}, ~1.2 ms^{-1} and ~1 ms^{-1}, respectively.

Table 2

Summary of the statistics by altimeter mission using swath and gridded scatterometer as ground-truth reference. Mean bias, RMSE, MAE, Pearson's correlation coefficient (ρ) and standard deviation along with the number of collocated data points and outliers are provided. The wind speed is classified as: low (<4 ms^{-1}), medium (4–10 ms^{-1}) and high (>10 ms^{-1}). Statistics are obtained outside the coastal area (50–300 km offshore).

Validation	Dates	Range	Length		Outliers		ρ	Bias	RMSE	MAE	STD		Mean	
			ALT	SCA							ALT	SCA	ALT	SCA
Altimeter ENVISAT vs. scatterometer (swath)	2003-01-01–2009-12-31	All	**62,110 (22.6%)**		**3532**	5.4%	0.96	−0.40	0.89	0.74	2.64	2.80	6.08	6.48
		<4	13,491 (21.7%)	11,959 (19.3%)	851	24.1%	0.69	−0.35	0.91	0.74	0.88	0.87	2.68	2.69
		4–10	43,460 (70.0%)	42,964 (69.2%)	2465	69.8%	0.91	−0.42	0.87	0.72	1.53	1.60	6.50	6.70
		≥ 10	5159 (8.3%)	7187 (11.6%)	216	6.1%	0.75	−0.35	1.04	0.83	1.23	1.31	11.46	11.50
Altimeter ENVISAT vs. scatterometer (gridded)		All	**260,704 (94.7%)**		**14,711**	5.3%	0.90	−0.29	1.22	0.96	2.66	2.47	6.11	6.40
		<4	54,695 (21.0%)	41,957 (16.1%)	2881	19.6%	0.54	−0.95	1.51	1.20	0.91	0.85	2.65	2.85
		4–10	183,658 (70.4%)	196,922 (75.5%)	10,520	71.5%	0.79	−0.21	1.08	0.87	1.51	1.51	6.48	6.60
		≥ 10	22,351 (8.6%)	21,825 (8.4%)	1310	8.9%	0.57	0.65	1.54	1.20	1.30	1.14	11.58	11.40
Altimeter SARAL vs. scatterometer (swath)	2013-03-14–2016-01-16	All	**30,375 (24.8%)**		**1702**	5.3%	0.94	−0.20	0.98	0.79	2.52	2.82	6.33	6.52
		<4	5238 (17.2%)	5513 (18.1%)	283	16.6%	0.52	0.01	1.10	0.90	0.79	0.89	2.98	2.67
		4–10	22,395 (73.7%)	21,364 (70.3%)	1336	78.5%	0.87	−0.20	0.93	0.75	1.58	1.56	6.49	6.66
		≥ 10	2742 (9.0%)	3498 (11.5%)	83	4.9%	0.81	−0.59	1.10	0.88	1.15	1.46	11.44	11.78
Altimeter SARAL vs. scatterometer (gridded)		All	**115,754 (94.6%)**		**6579**	5.4%	0.91	−0.12	1.07	0.86	2.57	2.56	6.17	6.29
		<4	22,092 (19.1%)	21,303 (18.4%)	1423	21.6%	0.57	−0.42	1.18	0.96	0.89	0.93	2.76	2.74
		4–10	83,844 (72.4%)	84,749 (73.2%)	4684	71.2%	0.82	−0.09	1.02	0.82	1.56	1.50	6.45	6.58
		≥ 10	9818 (8.5%)	9702 (8.4%)	472	7.2%	0.67	0.32	1.27	1.00	1.10	1.18	11.39	11.50
Altimeter Jason-1 vs. scatterometer (swath)	2002-01-01–2008-12-31	All	**19,748 (5.4%)**		**1564**	7.3%	0.97	−0.85	1.09	0.94	2.48	2.71	5.87	6.72
		<4	3938 (19.9%)	2900 (14.7%)	208	13.3%	0.81	−0.50	0.76	0.63	0.85	0.74	2.92	2.97
		4–10	14,323 (72.5%)	14,373 (72.8%)	1267	81.0%	0.93	−0.93	1.15	1.01	1.54	1.58	6.10	6.61
		≥ 10	1487 (7.5%)	2475 (12.5%)	89	5.7%	0.87	−0.92	1.20	1.05	1.36	1.48	11.47	11.70
Altimeter Jason-1 vs. scatterometer (gridded)		All	**345,836 (94.3%)**		**20,910**	5.7%	0.89	−0.75	1.37	1.13	2.42	2.43	5.89	6.64
		<4	67,995 (19.7%)	44,495 (12.9%)	4357	20.8%	0.43	−1.08	1.59	1.31	0.82	0.70	2.93	3.08
		4–10	253,124 (73.2%)	267,308 (77.3%)	15,323	73.3%	0.79	−0.73	1.32	1.10	1.50	1.54	6.15	6.62
		≥ 10	24,717 (7.1%)	34,033 (9.8%)	1230	5.9%	0.64	0.01	1.25	0.98	1.26	1.23	11.44	11.41
Altimeter Jason-2 vs. scatterometer (swath)	2009-01-01–2015-12-31	All	**13,262 (4.1%)**		**1110**	7.7%	0.98	−0.50	0.75	0.64	2.47	2.67	6.01	6.51
		<4	2627 (19.8%)	2298 (17.3%)	144	13.0%	0.84	−0.19	0.58	0.47	0.85	0.84	2.85	2.78
		4–10	9733 (73.4%)	9455 (71.3%)	872	78.6%	0.96	−0.57	0.78	0.67	1.63	1.58	6.38	6.64
		≥ 10	902 (6.8%)	1509 (11.4%)	94	8.5%	0.91	−0.70	0.84	0.76	1.00	1.11	11.24	11.36
Altimeter Jason-2 vs. scatterometer (gridded)		All	**307,583 (94.3%)**		**18,686**	5.7%	0.91	−0.38	1.12	0.91	2.46	2.43	5.98	6.36
		<4	60,826 (19.8%)	48,495 (15.8%)	3769	20.2%	0.47	−0.70	1.32	1.08	0.83	0.81	2.89	2.93
		4–10	224,123 (72.9%)	232,904 (75.7%)	13,736	73.5%	0.82	−0.35	1.06	0.86	1.53	1.50	6.27	6.51
		≥ 10	22,634 (7.4%)	26,184 (8.5%)	1181	6.3%	0.60	0.20	1.20	0.95	1.15	1.07	11.38	11.35

3.1.3. Calibration

This stage consists in a linear regression analysis to derive the correction coefficients for the altimeter estimates of the wind speed, in order to increase the agreement between scatterometer and altimeter. Similar procedures were applied for various regions in the past using buoys as the ground-truth reference (Desai and Vincent, 2003; Ray and Beckley, 2003; Queffeulou, 2003; Abdalla, 2006; Zieger et al., 2009). In our region of interest, we do not have access to any buoy data and available airport meteorological data are too far inland, so that our reference data were provided by the scatterometers. The slope and offset of the best linear fit between the scatterometer (L2-swath) data and the altimeter data in the off shore region (i.e. excluding the 50-km width coastal band) provides the calibration parameters by mission. The altimeter U_{10} data are taken as the independent variable. Then the calibrated wind speed (U_{10}^c) can be written as follows:

$$U_{10}^c = U_{10} \times slope + offset \tag{3}$$

The suitability of the calibration coefficients was evaluated matching the calibrated altimeter winds against both scatterometer products, repeating the same statistical analysis performed in the previous validation phase. The calibration procedure was successful in removing the negative bias, reducing the errors and increasing the match between the Probability Distribution Functions (PDF) of the scatterometer and the altimeter data (not shown). However there are slightly increased densities of medium wind conditions for the altimeter data in comparison with the scatterometer data. Such values are mostly present in ENVISAT and Jason-1 wind estimates. Table 3 provides the calibration results by satellite mission and Fig. 3 illustrates a typical calibration result for the Jason-2 altimeter data.

3.1.4. Time window differences

To quantify the impact of the relaxed temporal proximity between altimeter-scatterometer (L2-swath) for the ENVISAT/SARAL missions we apply the same temporal window (120–240 min) to the Jason-1/Jason-2 winds. The statistics for the validation experiments exhibit lower correlation coefficients (0.94 vs. 0.97/0.96 vs. 0.98) and higher bias (-0.87 ms^{-1} vs. -0.85 ms^{-1}/-0.54 ms^{-1} vs. -0.50 ms^{-1}) and RMS (1.26 ms^{-1} vs. 1.09 ms^{-1}/0.95 ms^{-1} vs. 0.75 ms^{-1}) values with regard to the former time criteria (60 min), for Jason-1/Jason-2 respectively. For the calibration the results were: correlation coefficients (0.94 vs. 0.97/0.96 vs. 0.98), bias (-0.12 ms^{-1} vs. -0.09 ms^{-1}/-0.09 ms^{-1} vs. -0.07 ms^{-1}) and RMS (0.90 ms^{-1} vs. 0.67 ms^{-1}/0.76 ms^{-1} vs. 0.53 ms^{-1}).

Finally, in order to gain confidence in the calibration within the blind zone, we have paired the L2-swath scatterometer data with the altimeter data for the nearest points from the coast (0–50 km). Our analysis indicates that statistics are comparable, although with slightly reduced scores relative to those performed offshore. The statistics are listed in Table 4.

3.1.5. Gridding, averaging and track selection

The calibrated wind speeds U_{10}^c were converted to neutral wind stress (τ) using the bulk formula:

$$\tau = \rho_a \times C_d \times \left(U_{10}^c\right)^2 \tag{4}$$

with ρ_a the constant air density (1.22 kg$\times$m^{-3}) and C_d the neutral drag coefficient varying with U_{10}^c as in Large and Pond (1981) and Gill (1982).

For each altimetry mission, data were first stacked into along-track cells of 7 km of length during the complete observation period considered in this study, similarly to what was done by Blarel et al. (2015) and Frappart et al. (2016). Altimetry data location in longitude and

Table 3

Calibration functions and statistics: The superscript "c" denotes the calibrated wind speed (U_{10}^c). Mean bias, RMSE, MAE, Pearson's correlation coefficient (ρ) and standard deviation along with the number of collocated concurrent data points and outliers are provided. Statistics are obtained outside the coastal area (50–300 km offshore).

Calibration	Calibration function/dates	Range	Length ALT	SCA	Outliers		ρ	Bias	RMSE	MAE	STD ALT	SCA	Mean ALT	SCA
Altimeter ENVISAT	$U_{10}^c = 1.0162*U_{10}+0.3031$/[2003-	**All**	**62,370 (23%)**		**3272**	**5.0%**	**0.96**	**−0.06**	**0.79**	**0.63**	**2.68**	**2.80**	**6.49**	**6.55**
vs. scatterometer	01-01, 2009-12-31]	<4	11,163 (17.9%)	11,511 (18.5%)	705	21.5%	0.64	−0.08	0.84	0.68	0.78	0.88	2.76	2.70
(swath)		4–10	44,666 (71.6%)	43,392 (69.6%)	2271	69.4%	0.91	−0.08	0.75	0.61	1.54	1.61	6.67	6.72
		≥ 10	6541 (10.5%)	7467 (12.0%)	296	9.0%	0.79	0.04	0.91	0.71	1.29	1.31	11.56	11.49
Altimeter ENVISAT		**All**	**260,606 (95%)**		**14,809**	**5.4%**	**0.90**	**0.07**	**1.21**	**0.93**	**2.71**	**2.48**	**6.50**	**6.43**
vs. scatterometer		<4	45,325 (17.4%)	41,099 (15.8%)	2326	15.7%	0.49	−0.69	1.38	1.07	0.81	0.85	2.73	2.85
(gridded)		4–10	187,328 (71.9%)	197,263 (75.7%)	10,861	73.3%	0.79	0.10	1.05	0.83	1.51	1.52	6.64	6.62
		≥ 10	27,953 (10.7%)	22,244 (8.5%)	1622	11.0%	0.60	1.04	1.74	1.36	1.39	1.14	11.69	11.41
Altimeter SARAL	$U_{10}^c = 1.0546*U_{10}-0.1438$/[2013-	**All**	**30,426 (25%)**		**1651**	**5.1%**	**0.94**	**−0.03**	**0.95**	**0.76**	**2.67**	**2.84**	**6.54**	**6.57**
vs. scatterometer	03-14, 2016-01-16]	<4	4936 (16.2%)	5430 (17.8%)	259	15.7%	0.51	0.02	1.10	0.90	0.82	0.89	2.93	2.67
(swath)		4–10	22,142 (72.8%)	21,377 (70.3%)	1309	79.3%	0.87	−0.02	0.91	0.73	1.60	1.56	6.57	6.67
		≥ 10	3348 (11.0%)	3619 (11.9%)	83	5.0%	0.82	−0.13	0.95	0.73	1.29	1.46	11.61	11.79
Altimeter SARAL		**All**	**115,711 (95%)**		**6622**	**5.4%**	**0.91**	**0.04**	**1.10**	**0.88**	**2.71**	**2.57**	**6.35**	**6.31**
vs. scatterometer		<4	21,007 (18.2%)	21,143 (18.3%)	1367	20.6%	0.56	−0.43	1.19	0.97	0.91	0.93	2.70	2.74
(gridded)		4–10	82,638 (71.4%)	84,717 (73.2%)	4678	70.6%	0.81	0.06	1.02	0.82	1.58	1.50	6.52	6.59
		≥ 10	12,066 (10.4%)	9851 (8.5%)	577	8.7%	0.70	0.76	1.44	1.11	1.24	1.20	11.54	11.51
Altimeter Jason-1	$U_{10}^c = 1.0631*U_{10}+0.4770$/[2002-	**All**	**20,363 (6%)**		**949**	**4.5%**	**0.97**	**−0.09**	**0.67**	**0.54**	**2.62**	**2.73**	**6.75**	**6.84**
vs. scatterometer	01-01, 2008-12-31]	<4	2293 (11.3%)	2801 (13.8%)	108	11.4%	0.72	0.06	0.60	0.48	0.73	0.73	2.97	2.98
(swath)		4–10	15,573 (76.5%)	14,886 (73.1%)	759	80.0%	0.93	−0.14	0.67	0.54	1.49	1.60	6.49	6.69
		≥ 10	2497 (12.3%)	2676 (13.1%)	82	8.6%	0.90	0.07	0.72	0.57	1.54	1.55	11.81	11.72
Altimeter Jason-1		**All**	**347,690 (95%)**		**19,055**	**5.2%**	**0.89**	**−0.01**	**1.18**	**0.93**	**2.56**	**2.44**	**6.72**	**6.73**
vs. scatterometer		<4	40,673 (11.7%)	41,831 (12.0%)	2401	12.6%	0.31	−0.70	1.40	1.12	0.70	0.69	3.01	3.10
(gridded)		4–10	266,002 (76.5%)	269,825 (77.6%)	14,444	75.8%	0.79	−0.04	1.07	0.86	1.46	1.55	6.51	6.67
		≥ 10	41,015 (11.8%)	36,034 (10.4%)	2210	11.6%	0.69	0.88	1.52	1.21	1.46	1.24	11.76	11.42
Altimeter Jason-2	$U_{10}^c = 1.0621*U_{10}+0.1304$/[2009-	**All**	**13,566 (4%)**		**806**	**5.6%**	**0.98**	**−0.07**	**0.53**	**0.43**	**2.63**	**2.70**	**6.56**	**6.64**
vs. scatterometer	01-01, 2015-12-31]	<4	2048 (15.1%)	2207 (16.3%)	118	14.6%	0.81	0.07	0.55	0.45	0.81	0.83	2.85	2.79
(swath)		4–10	9959 (73.4%)	9686 (71.4%)	618	76.7%	0.95	−0.11	0.53	0.43	1.60	1.59	6.57	6.69
		≥ 10	1559 (11.5%)	1673 (12.3%)	70	8.7%	0.92	−0.02	0.47	0.38	1.18	1.12	11.40	11.38
Altimeter Jason-2		**All**	**307,991 (94%)**		**18,278**	**5.6%**	**0.91**	**0.04**	**1.09**	**0.87**	**2.60**	**2.44**	**6.46**	**6.42**
vs. scatterometer		<4	47,612 (15.5%)	46,612 (15.1%)	2806	15.4%	0.40	−0.50	1.25	1.02	0.79	0.81	2.90	2.95
(gridded)		4–10	227,131 (73.7%)	234,111 (76.0%)	13,545	74.1%	0.81	0.04	0.99	0.79	1.51	1.51	6.46	6.54
		≥ 10	33,248 (10.8%)	27,268 (8.9%)	1927	10.5%	0.65	0.84	1.46	1.17	1.31	1.08	11.58	11.36

latitude of each cell was obtained as the mean the whole data during the whole study period. Monthly averages, mean seasonal cycles and total means of U_{10}^c and τ were subsequently computed by cell. Because the distance from the shore to the nearest cell varies between 3 and 10 km depending on the track/mission, we decided to interpolate the data to a common 5-km grid. The interpolated value at a query point is based on linear interpolation of the values at neighboring grid points. The points outside the domain were extrapolated using the same method. The resulting datasets provide information with enough resolution for documenting the surface atmospheric circulation in the coastal areas, which is addressed in the followings sections.

Considering the primary focus of the present work, i.e., the cross-shore wind reduction near the coastal zone, we have selected a subset of altimeter tracks searching the best approximations to orthogonal transects across the coastline (Wang et al., 2011; Pickett and Paduan, 2003). Table 5 provides the detail of the selected 200-km track segments (see right hand panels in Fig. 6a and b), including the coastal incident latitude, coastline direction angle (θ), track direction angle and orthogonal angular difference (ε) depicted in Fig. 5a. The coastline direction was calculated for each track using the tangent at the shoreline points within ~0.5° width segments around the incident latitude, as in Dewitte et al. (2011) or Pickett and Paduan (2003), based on the high-resolution (200-meter) shoreline database: Global Self-consistent, Hierarchical, High-resolution Geography Database (GSHHS). Although these formulations present a low difference in angle with respect to real orthogonal transects, they offer the possibility to compare objectively the shoreward wind drop-off at different latitudes.

Fig. 4a presents the mean state of the wind speed with superimposed arrows showing the mean wind speed and direction as derived from the QuikSCAT–ASCAT satellite data calculated over 2000–2014. Note that the mean wind direction is nearly parallel to the coastline. The variance for daily intraseasonal anomalies of the wind speed is displayed in Fig. 4b. Intraseasonal anomalies are calculated following Lin et al. (2000). It consists in first calculating the monthly means of the daily time series and then interpolating them back to a daily temporal grid using spline functions. The result is then retrieved from the original time series to derive daily intraseasonal anomalies.

Noteworthy, the region of interest experiences a large variability in the alongshore winds at intraseasonal timescales as illustrated in Fig. 4b, resulting in the intensification of surface winds at time periods near 10–25 days and 35–60 days (Rutllant et al., 2004; Renault et al.,

2009; Dewitte et al., 2011). This variability corresponding to periods shorter than twice the repeat cycle of the satellite (35 days and 10 days for ENVISAT/SARAL and Jason-1/Jason-2, respectively) will alias into the altimeter wind speed (Tierney et al., 2000), leading to uncertainty in the estimate of the low frequency variability, including the seasonal cycle. This issue will be addressed in Section 5.

3.2. Estimate of the wind drop-off scale

In order to characterize the shoreward decrease in wind speed, we define a wind drop-off scale (L_d) following Renault et al. (2015). This scale is obtained along the satellite track by estimating the cross-shore rate of change of the wind speed from a certain coastal distance L_d. The drop-off index DO_G is thus estimated as:

$$DO_G(lat) = 100 * \left[\frac{U_{10}^c(L_d, lat) - U_{10}^c(0, lat)}{U_{10}^c(L_d, lat)} \right] \qquad (5)$$

where lat is the incident latitude of the track at the coast, $U_{10}^c(L_d, lat)$ and $U_{10}^c(0, lat)$ are the wind speed estimates from the altimeter at the given distance L_d and at the grid point nearest to the coast respectively. The coastal wind speed $U_{10}^c(0, lat)$ is estimated as the average of the wind between 10 km offshore and the coast. The distance L_d, is estimated by defining a threshold value for the mean wind curl beyond which we are no longer within the drop-off zone. This value (negative in the Southern Hemisphere) is chosen at -1.8×10^{-5} s^{-1} which leads to L_d ranging from 10 to 150 km. Note that although such threshold is rather arbitrary, it corresponds to the distance from the coast beyond which the wind curl show very small offshore variability. Note also that Renault et al. (2015) use a larger value (3×10^{-5} s^{-1}, positive in Northern Hemisphere) for the threshold of mean wind curl to derive L_d along the US west coast, since they address the seasonal variability of the wind drop-off along the coast with model data instead of observations.

The estimation of the alongshore wind stress curl from the altimeter data requires assuming some mean wind direction considering that the altimeter only provides the wind amplitude. Since along the Chile/Peru coast the winds are predominantly oriented alongshore from about 40°S to the equator (Hill et al., 1998; Aguirre et al., 2012; Rahn, 2012), as illustrated in Fig. 4a, we derive a mean angle for the wind direction that is based on the already described coastline direction angle θ. In
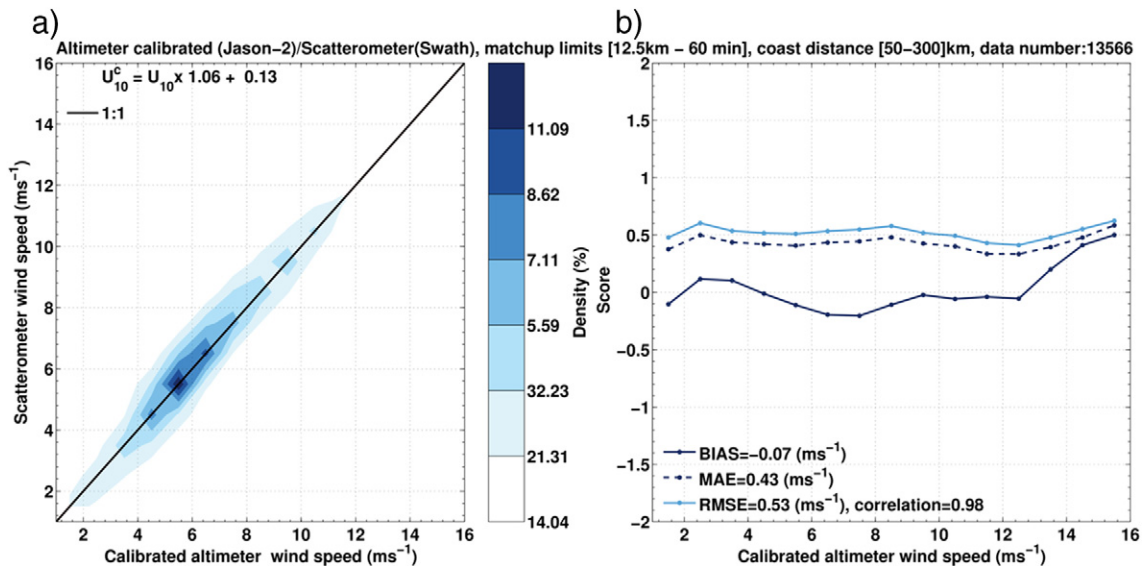

Fig. 3. Calibration result for Jason-2: (a) scatter density plot (shading), (b) mean bias, MAE, RMSE as function of the magnitude of the wind speed (divided in 16 bins). The correlation between the calibrated winds derived from Jason-2 and the swath scatterometer data is provided in panel (b). Statistics are obtained outside the coastal area (50–300 km offshore).

Table 4
Summary of the statistics by altimeter mission using swath scatterometer as ground-truth reference within the first 50 km off the coast. The statistics for the calibrated winds consider the calibration functions given in Table 3.

Validation/calibration 0–50 km off the coast	Dates	Range	Length ALT	Length SCA	Outliers		ρ	Bias	RMSE	MAE	STD ALT	STD SCA	Mean ALT	Mean SCA
Altimeter ENVISAT vs. scatterometer (swath)	2003-01-01–2009-12-31	**All**	**10,513 (94.4%)**		**621**	**5.6%**	**0.92**	**−0.55**	**1.16**	**0.94**	**2.55**	**2.65**	**4.75**	**5.30**
		<4	4603 (43.8%)	3739 (35.6%)	282	45.4%	0.59	−0.68	1.21	0.97	0.88	0.84	2.52	2.71
		4–10	5533 (52.6%)	6135 (58.4%)	319	51.4%	0.85	−0.47	1.11	0.91	1.52	1.58	6.14	6.24
		≥ 10	377 (3.6%)	639 (6.1%)	20	3.2%	0.66	−0.26	1.40	1.12	1.51	1.40	11.59	11.45
Calibrated altimeter ENVISAT vs. scatterometer (swath)		**All**	**10,499 (94.3%)**		**635**	**5.7%**	**0.93**	**−0.23**	**1.03**	**0.83**	**2.59**	**2.66**	**5.12**	**5.34**
		<4	4031 (38.4%)	3671 (35.0%)	238	37.5%	0.54	−0.41	1.07	0.85	0.78	0.84	2.66	2.72
		4–10	5976 (56.9%)	6172 (58.8%)	370	58.3%	0.86	−0.12	0.98	0.79	1.55	1.58	6.24	6.24
		≥ 10	492 (4.7%)	656 (6.2%)	27	4.3%	0.69	0.02	1.31	1.05	1.54	1.43	11.62	11.48
Altimeter SARAL vs. scatterometer (swath)	2013-03-14–2016-01-16	**All**	**3041 (93.5%)**		**212**	**6.5%**	**0.92**	**−0.21**	**1.11**	**0.91**	**2.48**	**2.74**	**5.54**	**5.75**
		<4	882 (29.0%)	870 (28.6%)	53	25.0%	0.52	−0.18	1.09	0.89	0.81	0.87	2.88	2.68
		4–10	2000 (65.8%)	1915 (63.0%)	145	68.4%	0.84	−0.22	1.13	0.94	1.65	1.61	6.25	6.40
		≥ 10	159 (5.2%)	256 (8.4%)	14	6.6%	0.84	−0.28	1.08	1.06	1.01	1.06	11.31	11.31
Calibrated altimeter SARAL vs. scatterometer (swath)		**All**	**3044 (93.6%)**		**209**	**6.4%**	**0.92**	**−0.08**	**1.09**	**0.90**	**2.62**	**2.76**	**5.70**	**5.78**
		<4	836 (27.5%)	864 (28.4%)	50	23.9%	0.50	−0.16	1.10	0.90	0.83	0.86	2.83	2.67
		4–10	1991 (65.4%)	1916 (62.9%)	144	68.9%	0.83	−0.08	1.11	0.92	1.67	1.61	6.28	6.42
		≥ 10	217 (7.1%)	264 (8.7%)	15	7.2%	0.82	0.17	0.83	0.64	1.15	1.08	11.37	11.32
Altimeter Jason-1 vs. scatterometer (swath)	2002-01-01–2008-12-31	**All**	**3343 (92.5%)**		**209**	**5.9%**	**0.96**	**−0.86**	**1.19**	**1.01**	**2.66**	**2.81**	**5.15**	**6.01**
		<4	1185 (35.4%)	864 (25.8%)	50	23.9%	0.70	−0.72	1.03	0.85	0.85	0.71	2.76	2.99
		4–10	1972 (59.0%)	2169 (64.9%)	144	68.9%	0.90	−0.96	1.24	1.08	1.53	1.57	5.93	6.36
		≥ 10	186 (5.6%)	310 (9.3%)	15	7.2%	0.81	−0.62	1.55	1.27	2.23	2.04	12.18	12.02
Calibrated altimeter Jason-1 vs. scatterometer (swath)		**All**	**3395 (93.9%)**		**220**	**6.1%**	**0.96**	**−0.15**	**0.82**	**0.65**	**2.80**	**2.84**	**5.97**	**6.11**
		<4	802 (23.6%)	840 (24.7%)	57	25.9%	0.60	−0.21	0.77	0.61	0.70	0.71	2.91	2.99
		4–10	2268 (66.8%)	2212 (65.2%)	147	66.8%	0.91	−0.17	0.78	0.64	1.47	1.59	6.17	6.39
		≥ 10	325 (9.6%)	343 (10.1%)	16	7.3%	0.86	0.17	1.16	0.85	2.18	2.00	12.08	11.95
Altimeter Jason-2 vs. scatterometer (swath)	2009-01-01–2015-12-31	**All**	**1498 (93.3%)**		**107**	**6.7%**	**0.97**	**−0.52**	**0.84**	**0.69**	**2.47**	**2.76**	**5.22**	**5.74**
		<4	492 (32.8%)	430 (28.7%)	25	23.4%	0.81	−0.25	0.63	0.51	0.87	0.81	2.88	2.88
		4–10	924 (61.7%)	933 (62.3%)	69	64.5%	0.94	−0.63	0.92	0.78	1.51	1.58	5.91	6.20
		≥ 10	82 (5.5%)	135 (9.0%)	13	12.1%	0.97	−0.58	1.58	1.51	1.58	1.51	11.58	11.68
Calibrated altimeter Jason-2 vs. scatterometer (swath)		**All**	**1525 (95.%)**		**80**	**5.0%**	**0.98**	**−0.11**	**0.63**	**0.51**	**2.66**	**2.82**	**5.74**	**5.86**
		<4	380 (24.9%)	420 (27.5%)	17	21.3%	0.76	0.04	0.61	0.48	0.84	0.81	2.89	2.87
		4–10	1017 (66.7%)	950 (62.3%)	58	72.5%	0.94	−0.17	0.65	0.53	1.52	1.59	6.05	6.23
		≥ 10	128 (8.4%)	155 (10.2%)	5	6.3%	0.94	−0.13	0.59	0.47	1.65	1.46	11.78	11.69

the following we will use a rotated coordinate system where x is perpendicular to the coast and y is along the coast, with positive y equatorward, as in Fig. 5a. Wind speed and wind stress vector components can therefore be written as:

$$U_x = \cos(\theta - \phi) * U_{10}^c; \quad U_y = \sin(\theta - \phi) * U_{10}^c \tag{6}$$

$$\tau x = \cos(\theta - \phi) * \tau; \quad \tau y = \sin(\theta - \phi) * \tau \tag{7}$$

where U_{10}^c is the wind speed, τ the wind stress, θ the coastal orientation angle, and ϕ the track angle. With the assumptions that mean winds are predominantly alongshore, the along-track wind stress curl is the x derivative of the wind stress (e.g. Figueroa and Moffat, 2000). This hypothesis was tested from the mean ERA-Interim and CFSR winds, which shows that the error in the estimation of the wind curl near the coast is <10% on average between 5°S and 40°S (not shown).

Another assumption consists in neglecting the angle between the track of the satellite and the x-direction, which is acceptable considering that we are focusing on a relatively short distance from the coast.

While DO_G provides a mean rate of alongshore wind change near the coast, it does not provide information on the shape of the along-shore wind variations as a function of the distance from the coast and on how the drop-off shape deviates from the linear fit of the horizontal wind profile. We thus define an index DO_I that characterizes the wind drop-off shape. It writes as follows:

$$DO_I(lat) = 100 * \left[\frac{\left(\int_{L_d}^0 U_{10}^c(x, lat)dx - \int_{L_d}^0 y(x)dx \right)}{\int_{L_d}^0 y(x)dx} \right] \tag{8}$$

where lat is the incident latitude of the track at the coast, $y(x)$ is the straight line from $(L_d, U_{10}^c(L_d, lat))$ to the nearest point to the coast

$(0, U_{10}^c(0, lat))$. Both integrals are calculated along the track using the trapezoidal method with dx equals to 5 km.

A negative/positive DO_I indicates a convex/concave horizontal wind profile. A concave horizontal profile would tend to locate the peak Ekman pumping close to the coast, which has implication in terms of the efficiency of the Ekman pumping in generating upwelling (Capet et al., 2004).

4. Results

4.1. Wind drop-off characterization

As a first step, we present Fig. 6a and b that display the mean wind speed for the altimeter and the scatterometer along the selected tracks for Jason-1/Jason-2 and SARAL/ENVISAT respectively. The data are shown for a 200-km coastal strip interpolated at a 5-km resolution. There is an overall good agreement between the altimeter and the scatterometer (i.e. RMS = 0.33, 0.28, 0.51 and 0.55 ms^{-1} for Jason-1/Jason-2 and ENVISAT/SARAL respectively) although discrepancies arise locally due in part to differences in repeat cycle, spatial resolution, and technology of the onboard instruments (see Table 1). Despite differences between products, the details of the circulation near the coast (i.e. between the coast and 50-km offshore) can be inferred from the altimeter data.

The most noticeable feature is the marked shoreward reduction in wind speed. This wind drop-off takes place at all latitudes independently of the offshore wind speed, although the reduction rate is latitudinally dependent. Observed wind speed differences between 100 km offshore and the coast are ubiquitous ranging between [1–2.5] ms^{-1} for Jason-1/Jason-2 and [0–4] ms^{-1} for ENVISAT/SARAL.

The coastal wind speed $U_{10}^c(0, lat)$ is illustrated for all the missions with long enough time periods (i.e. ENVISAT, Jason-1 and Jason-2) in

Table 5
Details of the selected tracks by mission including, number id, incident latitude at coast, track angle, coastline orientation angle and orthogonal difference (see Figs. 5 and 6a, b for illustration).

ENVISAT-SARAL

Track number	1	2	3	4	5	6	7	8	9	10	11	12	13	14	15	16	17	18	19	20	21	22	23	24	25	26	27	28	29	30	31
Latitude at coast (°S)	6.2°	6.6°	7.1°	8.1°	8.9°	10.0°	11.0°	11.9°	12.7°	14.1°	15.0°	15.5°	15.8°	16.3°	16.4°	–17°	–17°	–18°	–18°	–19°	–24°	–26°	–28°	–29°	–30°	–33°	–34°	–35°	–36°	–37°	–40°
Track angle	257°	257°	257°	257°	257°	257°	257°	257°	257°	257°	257°	257°	257°	257°	257°	256°	256°	256°	256°	256°	104°	104°	104°	104°	105°	105°	105°	106°	106°	106°	107°
Coastline angle	149°	147°	123°	133°	110°	113°	102°	109°	119°	121°	141°	148°	150°	153°	157°	151°	148°	141°	139°	102°	86°	84°	68°	67°	84°	66°	85°	49°	70°	47°	72°
Orthogonal difference	18°	21°	45°	34°	57°	54°	65°	58°	48°	46°	26°	18°	17°	13°	10°	15°	18°	26°	27°	64°	72°	70°	54°	53°	70°	50°	70°	33°	54°	31°	55°

Jason-1-Jason-2

Track number	1	2	3	4	5	6	7	8	9	10	11	12
Latitude at coast (°S)	–6.2°	–8.5°	–11.7°	–14.9°	–16.4°	–17.9°	–23.4°	–24.5°	–28.7°	–33.4°	–36.2°	–39.7°
Track angle	250°	249°	249°	248°	247°	247°	244°	113°	115°	118°	120°	122°
Coastline angle	144°	117°	123°	135°	155°	140°	94°	87°	69°	78°	69°	58°
Orthogonal difference	16°	42°	35°	23°	2°	17°	61°	64°	44°	51°	39°	26°
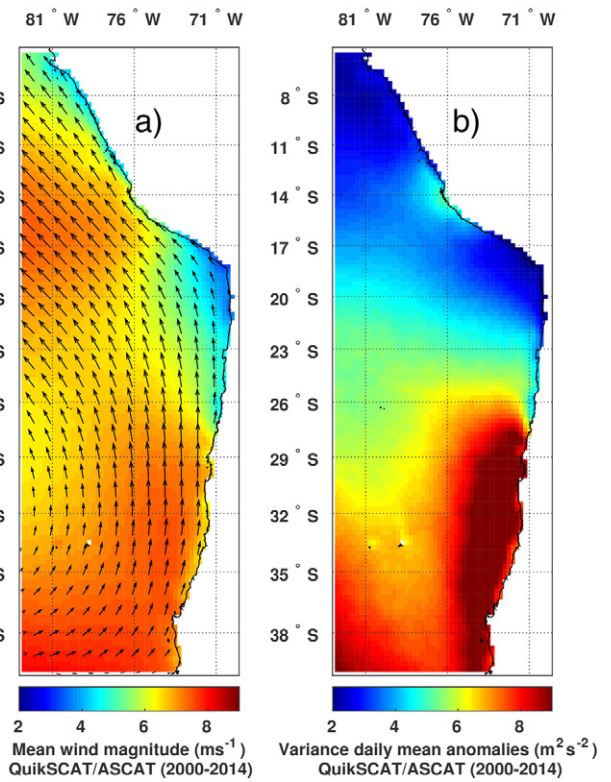
Fig. 4. (a) Mean surface wind speed and wind vectors. (b) Variance of daily intraseasonal anomalies. Intraseasonal anomalies are defined as departures from the monthly means (Lin et al., 2000). Data are from the gridded daily averages QuikSCAT-ASCAT (2000–2014).

Fig. 7a. There is an overall good agreement between the three altimeters although ENVISAT exhibits a larger alongshore variability, with in particular larger (weaker) coastal wind at 28°S (12°S), the region of the maximum (minimum) wind, with respect to Jason-1 and Jason-2.

In order to characterize the wind drop-off, the coastward decaying rate of along-shore wind is estimated (see Section 3.2 and Eq. (5) for DO_G definition). The DO_G index shows a significant latitudinal variability (Fig. 7b), out of phase with the coastal wind speeds $U_{10}^c(0, lat)$ (Fig. 7a). In particular, regions where the coastal jet is strong ($U_{10}^c(0, lat) > \sim 4 \ m \cdot s^{-1}$), between 34°S and 29°S off Chile and between 17°S and 13°S off Peru, correspond to low value of DO_G. Conversely, in regions of relatively weak coastal winds, DO_G is larger, reaching almost 80% off Callao at 12°S.

While DO_G is a linear estimate of the rate of cross-shore wind reduction, DO_I (Fig. 7c) provides a measure of the shape of this wind speed reduction from the offshore horizontal wind profile (see Section 3.2 and Eq. (8) for DO_I definition). In particular, it indicates where the steepest offshore wind decrease is located along the track. For instance, a large positive DO_I value (i.e. concave horizontal wind profile) indicates a position of the maximum wind stress close to the coast. While DO_I is highly correlated to DO_G (R = 0.89), it is negatively correlated to the outer offshore wind speeds (R = −0.70), indicating that when the wind is strong, the horizontal wind profile is more concave and the maximum wind curl moves closer to the coast. The apparent differences in variability of DO_G and DO_I between ENVISAT and Jason-1/Jason-2 can be explained in terms of the influence of coastline meandering on the wind drop-off. Since there are slight differences in the latitudes of the tracks between ENVISAT and Jason-1/Jason-2, winds can experience the effect of bays, promontories and small islands depending on the satellite and the incident latitude at the coast.

The wind drop-off has been also shown to be sensitive to the orography, which is prominent over the west coast of South America due to
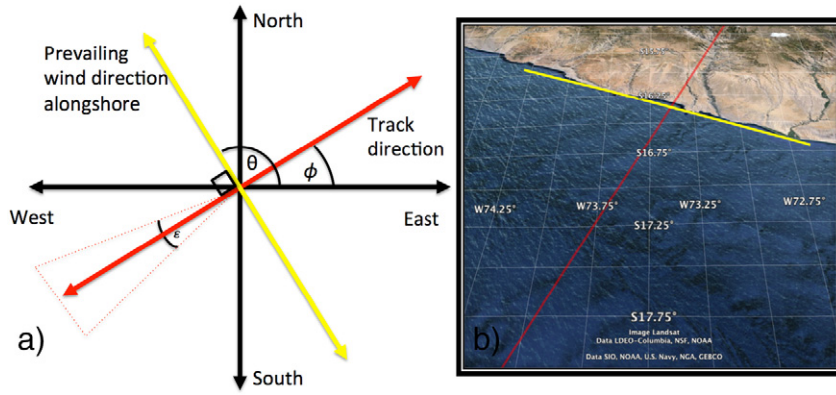
Fig. 5. (a) Coordinate systems used for the calculation: The x-axis (red) is in the cross-shore direction and the y-axis (yellow) is parallel to the shore direction, θ: the coastline angle, ϕ: the rotation angle and ε: the angular difference between the rotated x-axis and the ground track. (b) Map of the coast of Peru with the Jason-1/Jason-2 ground track (red line) that intersects the coast at 16.4°S. The yellow line is the tangent to the coastline. Note that the angular difference (ε) between the track of the satellite and the x-direction is neglected. (For interpretation of the references to colour in this figure legend, the reader is referred to the web version of this article.)

the presence of coastal mountain ranges. For the coast of California, based on sensitivity experiments with a regional atmospheric model, Renault et al. (2015) showed for instance that land shape could produce an enhanced drag coefficient for the low-level circulation that would result in a turbulent momentum flux divergence. The latter, combined to orographically-induced vortex stretching, would produce the wind drop-off. They defined an along-shore orography index (Hindex) as the mean orographic height over the strip of land within 100 km of the coast and show that is significantly correlated with the wind drop-off spatial length L_d. Here, while we also observe an overall agreement between meridional changes in DO_G and the coastal orographic height (i.e. the larger the Hindex, the weaker the wind at the coast, not shown), we did not evidence a significant linear relationship between Hindex and L_d, most likely due to the coarse meridional resolution of the altimetric wind data. On the other hand, the relationship between the coastline geometry, estimated from the GSHHS shoreline, and DO_G can be appreciated from a meandering index (Mindex). It consists of searching the local maxima and minima in the coastline longitude and imposing an amplitude threshold of 23 km for promontories and 4 km for bays. Fig. 7d shows the main filtered peaks along the coast as red circles for the main promontories and black circles for the main bays. It indicates that when there is a significant difference between ENVISAT and Jason-1/Jason-2 in DO_G (or coastal wind), it can be explained to some extent by the effect of a bay or a promontory. For instance, the Gulf of Arauco at 37.23°S (ENVISAT track N°30) experiences a notorious wind reduction and a high drop-off index explained by the abrupt change of the coastline orientation from N-S to E-W and favored by the presence of Santa María Island (73.52°W 37.03°S). Note that the ENVISAT track impinges inside the bay, which may explain the larger drop-off there. ENVISAT tracks at Punta Lengua de Vaca (30°S) and Punta Choros (29°S), on the other hand, indicate a large coastal wind and a weak wind drop-off compared to Jason-1/Jason-2, which might results from the alternation of promontories and bays. The difference in the repeat cycles and wind speed algorithms between ENVISAT and Jason-1/Jason-2 may also produce a residual effect on the mean at some locations. Due to the complexity of small scales processes (see Renault et al., 2015) in the near-coastal regions, the explanation of the differences between altimeter missions remains here qualitative and would require further studies using regional atmospheric modeling.

4.2. Transport and upwelling

The altimeter data offers the opportunity to estimate Ekman pumping and Ekman transport and compare their relative contributions to the vertical velocities and transports near the coast. The Ekman pumping vertical velocity, W, and the Ekman transport, M, were estimated following Pickett and Paduan (2003) who based it on Smith (1968) and Bakun (1973) as:

$$W = \frac{1}{\rho_w f} \nabla \times \tau \tag{9}$$

$$M = \frac{1}{\rho_w f} \tau \times \kappa \tag{10}$$

where $\nabla \times \tau$ is the along-track curl of the derived mean wind stress (obtained in Section 3.2) calculated as the along-track gradient of the alongshore wind. For Ekman transport (10) τ is the mean wind stress vector nearest to the coast, ρ_w is the density of seawater (assumed constant at 1024 kg m^{-3}), f is the Coriolis parameter; and κ is the unit vertical vector. The offshore component of the Ekman transport was calculated from the dot product of the above transport vector with a unitary vector orthogonal to the coastline (Pickett and Paduan, 2003).

In order to compare both upwelling processes, we had to convert Ekman pumping into vertical transport by integrating the vertical velocities over some offshore distance from the coast. Following former studies (Pickett and Paduan, 2003; Aguirre et al., 2012), we use a distance of 150 km from the coast, which corresponds to the maximum value of L_d estimated along the coast. The resulting vertical transports, for the different altimetry missions, are displayed in Fig. 8. It first shows an overall good agreement between the different satellite products for both Ekman transport (Fig. 8a) and pumping (Fig. 8b). The most prominent differences are observed around 12°S, 30°S and 37°S, with ENVISAT transport estimations differing from both Jason-1 and Jason-2. As mentioned earlier, they can be attributed both to the differences in repeat cycle and to the local presence of bays or promontories depending on the satellite incident latitude at the coast. Second, Fig. 8 indicates that the magnitudes of Ekman transport and pumping are comparable although there can be large differences locally at some latitudes sampled by ENVISAT (e.g. at ~29°S). The agreement is on average larger off Chile than off Peru where the transport associated with Ekman pumping is larger than Ekman transport (between 20°S and 7°S) by an average factor of ~1.4. Noteworthy, in a former study for the coast of California from regional atmospheric model outputs, Pickett and Paduan (2003) found comparable magnitudes and relative contributions of Ekman transport versus Ekman pumping, which is in agreement with our estimate. On the other hand, Aguirre et al. (2012) using QuikSCAT data found a much larger contribution of Ekman transport versus Ekman pumping for the central Chile region compared to our estimate. As mentioned

by these authors, the scatterometer data lead to an underestimation on the contribution of Ekman pumping.

Messié et al. (2009) have already mentioned that the caveats associated with the calculation of upwelling from the QuikSCAT data result from resolution and lack of nearshore pixels. However although the relative proportion of Ekman transport and pumping may be biased, the total transport should not change (Pickett and Paduan, 2003). This is what we observed here since the differences between satellite products are reduced when summing up the contributions of Ekman transport and pumping. The latitudinally-averaged standard deviation between products reduces to 0.09 for the total transport compared to 0.12 and 0.13 for Ekman transport and pumping respectively (units = m^3 s^{-1}

per meter of coast). In order to highlight the latitudinal variability between Ekman transport and pumping, Fig. 8d presents the results in the form of a histogram for Jason-2. Clearly, the Ekman pumping tends on average to dominate with respect to Ekman transport over the Peruvian coast north of 15°S, whereas over the central Chilean coast (33°S–27°S), Ekman transport is the dominant process. Fig. 8d also illustrates the large alongshore variability resulting from the intricate coastline (see Fig. 7d).

Similar comparison is done for the vertical velocity estimates associated with both Ekman pumping and transport. The vertical velocities resulting from Ekman transport are estimated using an upwelling scale (L_{cu}) of the order of ~10 to 5 km (from 5°S to 40°S), calculated
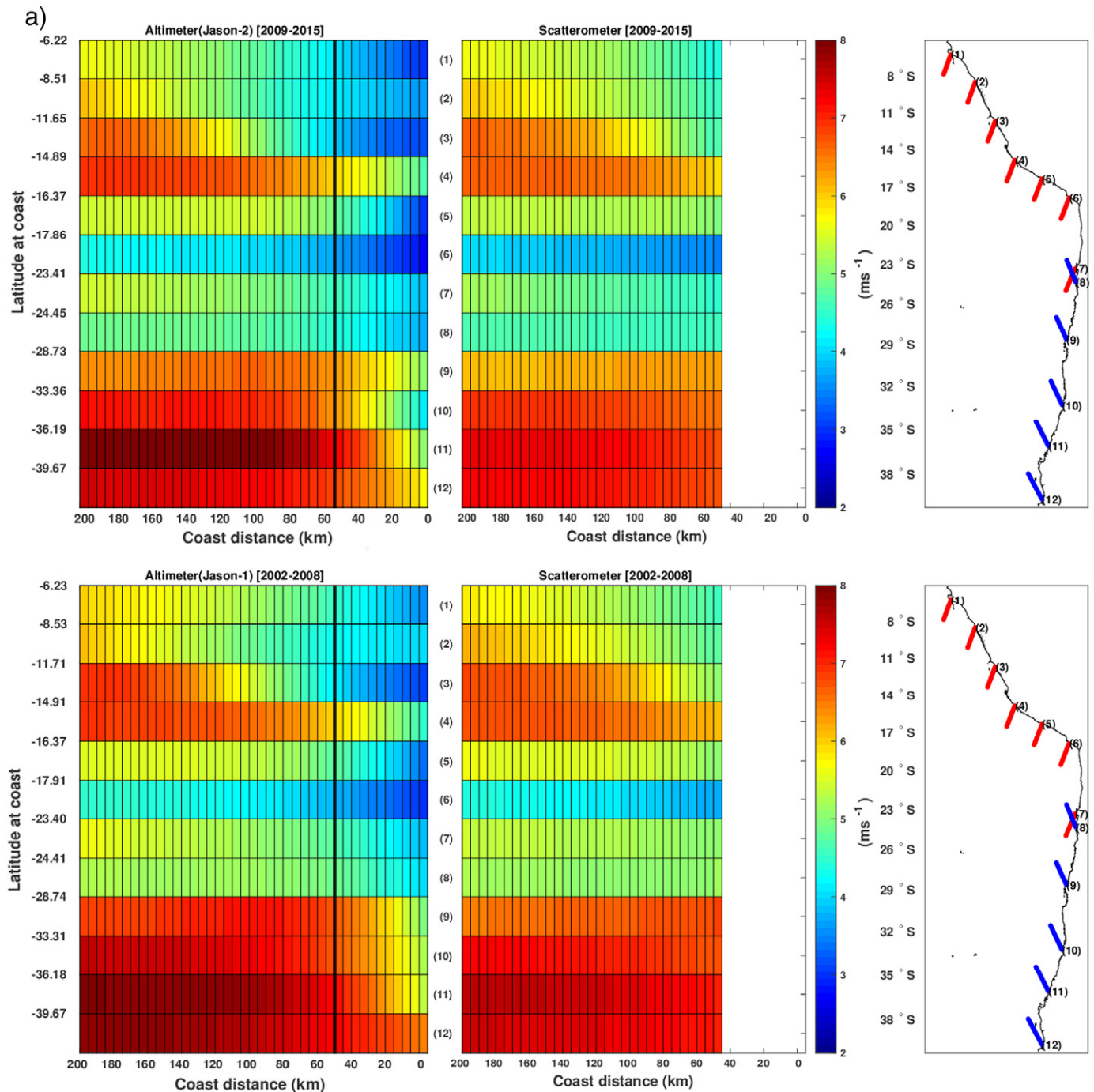
Fig. 6. a: Mean wind speed for Jason-1 and Jason-2 (left column) and scatterometer (middle column) calculated over the same periods. The vertical black lines on the left hand side panels indicate the offshore distance (50 km) defined as the limit for the scatterometer confidence. Reference maps (right hand panels) show the altimeter tracks positions by mission. b: Mean wind speed for ENVISAT and SARAL (left column) and scatterometer (middle column) calculated over the same periods.

b)
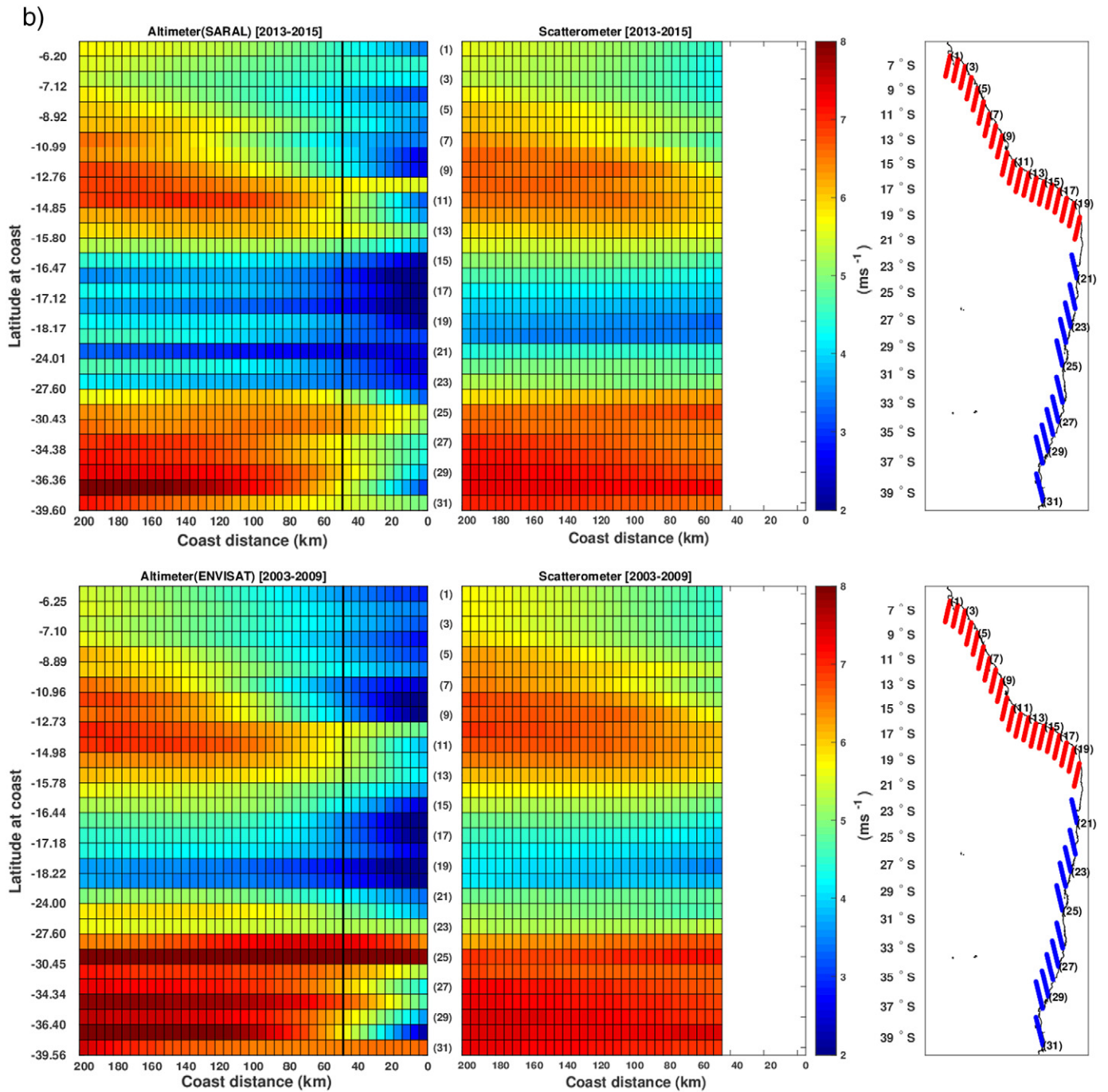
Fig. 6 (*continued*).

following Marchesiello and Estrade (2010) and Renault et al. (2012). The Ekman pumping vertical velocities are averaged within a 10-km width coastal band (10 km corresponding to the location where the maximum in Ekman Pumping is detected). The results of the comparison are presented in Fig. 9.

Differences between products are larger than those found for the estimates of transport due, on the one hand, to the larger sensitivity of the estimated velocity to the upwelling scale and to the assumed location of maximum upwelling, on the other hand. Here we consider, that the upwelling is confined to the frictional inner shelf zone where surface and Ekman bottom layers overlap, which implies that upwelling (i.e., where vertical velocities are maximum) is confined within 5 to 10 km from the coast (Marchesiello and Estrade, 2010). This results in a

different balance between both processes, with vertical velocities associated with Ekman transport having much larger amplitude than vertical velocities associated with Ekman pumping (Fig. 9a, b). However, this is not observed in the areas with a strong wind drop-off, which leads to a larger contribution of Ekman pumping velocity over Ekman transport vertical velocity (e.g. near 12°S). Fig. 9d illustrates the large alongshore variability of the relative contribution of vertical velocities induced by Ekman transport and pumping from the Jason-2 data.

5. Discussion and conclusions

In this study, we have documented the mesoscale atmospheric circulation along the coast of Peru and Chile from wind speed

altimeter data, motivated by the consideration that this circulation is not observable by the scatterometers (i.e. blind zone for the instrument) despite its potentially strong impact on the coastal oceanic circulation (Capet et al., 2004; Renault et al., 2012, 2016). We first presented the calibration method of the altimeter data, which is based on the comparison between the scatterometer and altimeter datasets outside the coastal area (50–300 km offshore). Statistically, the ocean surface winds from both instruments agree very

well, with high correlation coefficients and low bias and RMSE differences. The missions Jason-1 and Jason-2 exhibit higher scores with respect to scatterometer than the ENVISAT and SARAL missions. The calibration coefficients are inferred from the slope and offset of the regression between both altimeter and scatterometer data, with values consistent with those from former studies (Queffeulou, 2003; Zieger et al., 2009) (i.e. slopes near 1.00, small offsets and RMS errors less than 0.7 ms^{-1}).
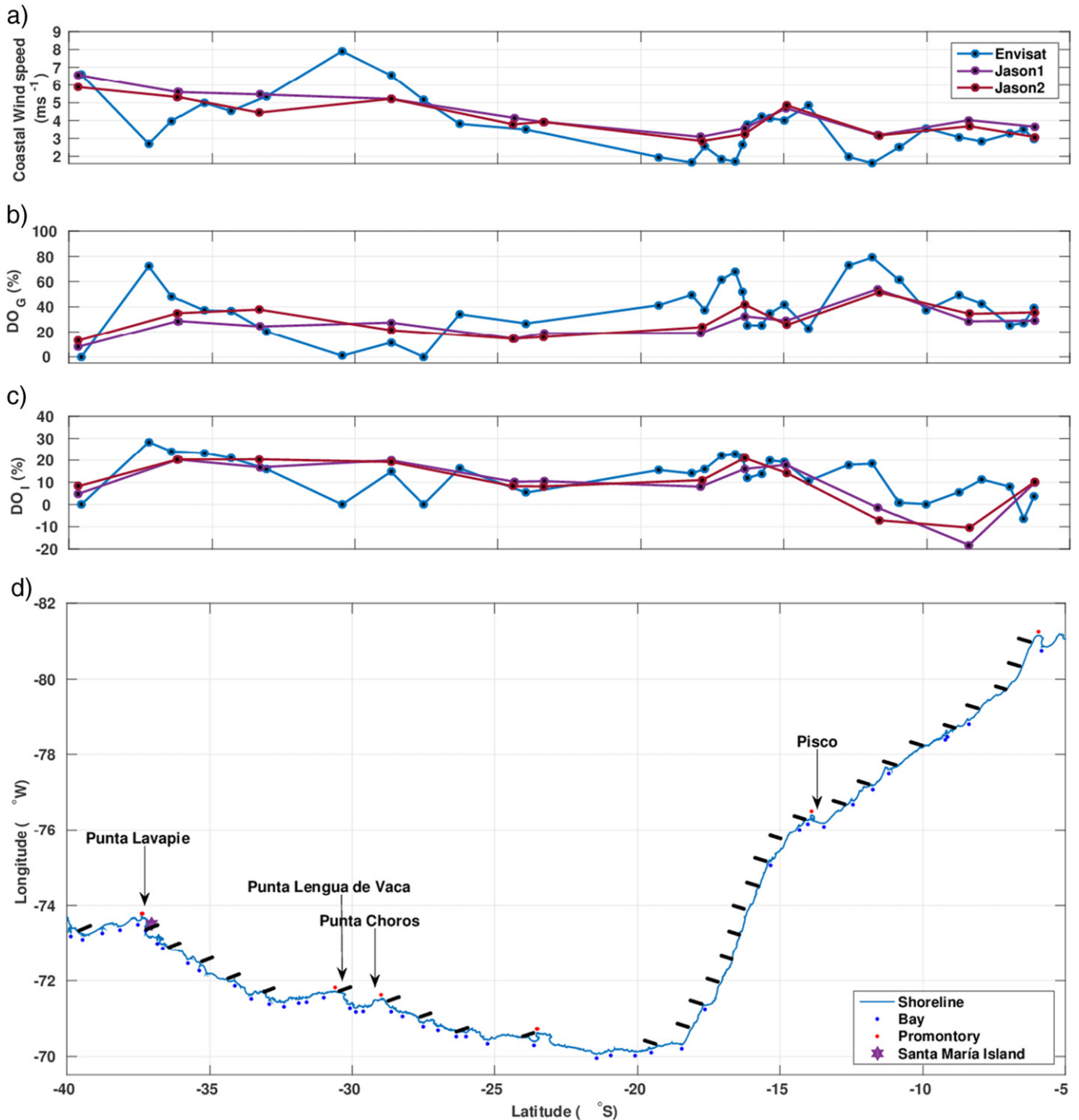
Fig. 7. (a) Coastal wind estimated as the average of the wind speed within the first 10 km off the coast. (b) Wind drop-off index (DO_G). (c) Drop-off shape index (DO_I). (d) Meandering index estimated performing a peak analysis to the coastal longitude. Red circles correspond to the main promontories whereas blue circles indicate the main bays. The black segments correspond to the ENVISAT tracks. Black arrows indicate the location of the main promontories at Punta Lavapie, Punta Lengua de Vaca, Punta Choros and Pisco. (For interpretation of the references to colour in this figure legend, the reader is referred to the web version of this article.)

Calibrated and gridded measurements were then used to characterize the mean state of the dominant alongshore flow and assess the along-track wind drop-off and its likely influence on coastal upwelling through Ekman pumping/transport. We find that the altimeter winds have the appropriate resolution for documenting the characteristics of the mean near-shore winds, highlighting in particular a significant alongshore variability of the wind drop-off. The latter tends to be larger at latitudes where the coastal winds are weak, which implies a dominant contribution of Ekman pumping with respect to Ekman transport there.

Differences between products (Jason-1/Jason-2 versus ENVISAT/SARAL) can be understood in terms of (i) the location where the satellite track impinges at the coast, revealing the influence of details in the coastline (bays and promontories), (ii) the differences in time sampling between the different missions (both the observation period and the sampling frequency), and (iii) the differences caused by the characteristics of the sensors, the frequency used and the algorithms used for processing the data.

While we have documented here the mean coastal circulation, we may wonder to which extend the altimeter data could help addressing the temporal variability in the wind drop-off, considering the significant intraseasonal wind variability in the region of interest (e.g. Renault et al., 2009; Dewitte et al., 2011; see also Fig. 4b). Here it is only expected

at best to be able to resolve the seasonal cycle. To evaluate this, the scatterometer and the calibrated altimeter data are compared in terms of the annual harmonics over the domain consisting in the fringe of 50 km from the coast and extending up to 100 km offshore. Results (Fig. 10) suggest that altimeter data near the coast could be used to document the seasonal cycle of the wind drop-off, although large differences between products can be observed locally, in particular off central Chile where the coastal jet experiences a significant intraseasonal variability (Renault et al., 2009) associated to its seasonal meridional migration (Garreaud and Muñoz, 2005), which is likely to result in more pronounced aliasing effect than off Peru. To reduce the uncertainties associated with these differences, these results would need to be combined with those from a regional modeling study to gain confidence in the satellite data products and provide a more quantitative physical explanation. This is planned for future work.

At this stage, we can note that the altimeter data are highly valuable for the regional modeling community interested in EBUS since they offer a benchmark dataset to validate regional atmospheric models in near coastal areas and investigate to which extent they can simulate the wind drop-off and its alongshore variability. These results can also help in assessing the optimal resolution of regional atmospheric models (convergence issues) and thus open the possibility to investigate
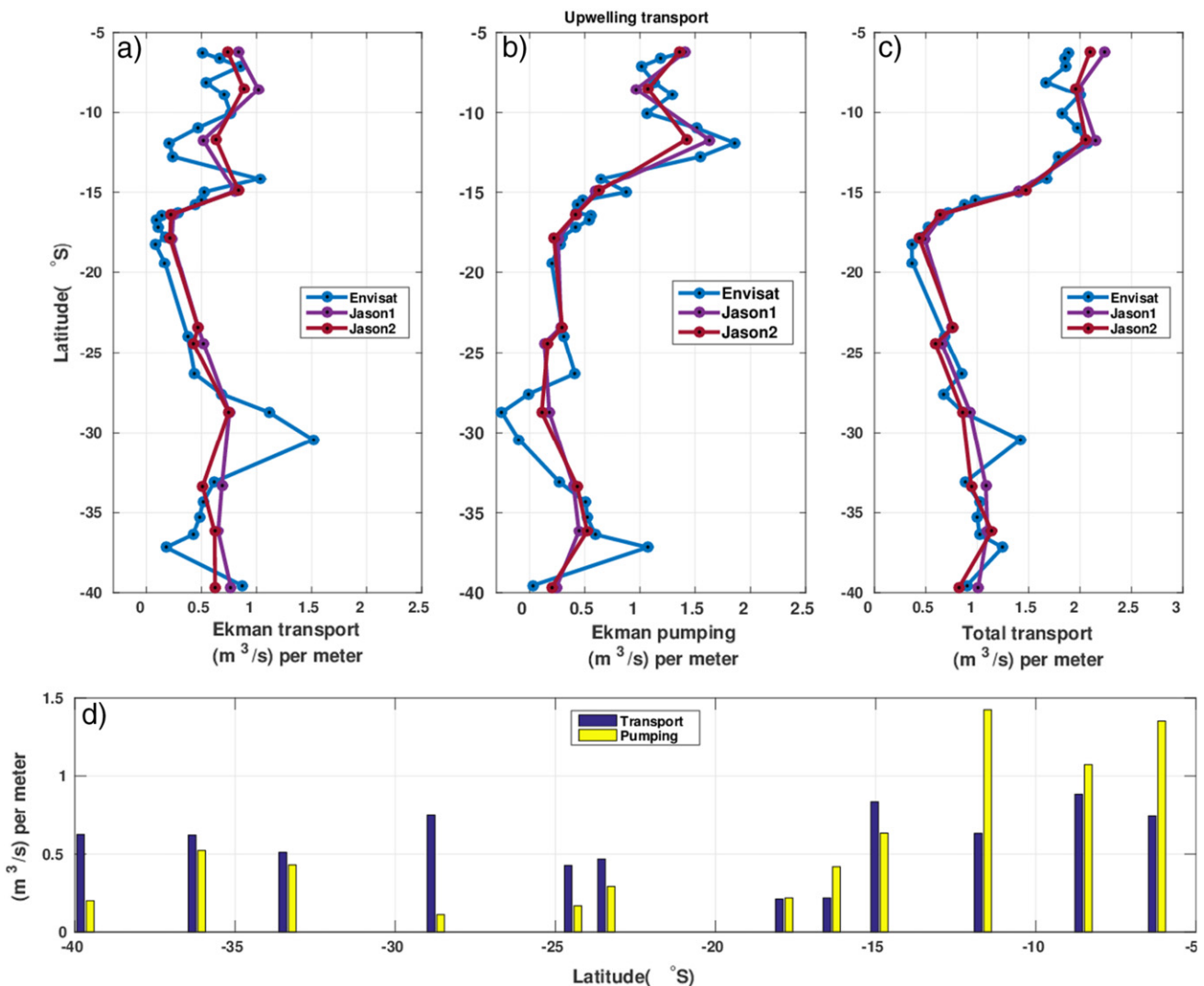

Fig. 8. Contribution of the Ekman transport (a) and Ekman pumping (b) to the mean vertical transport near the coast (within 150 km offshore). (c) Total transport (Ekman transport + Ekman pumping). (d) Comparative detail with the Jason-2 vertical transport associated with Ekman transport and Ekman pumping.
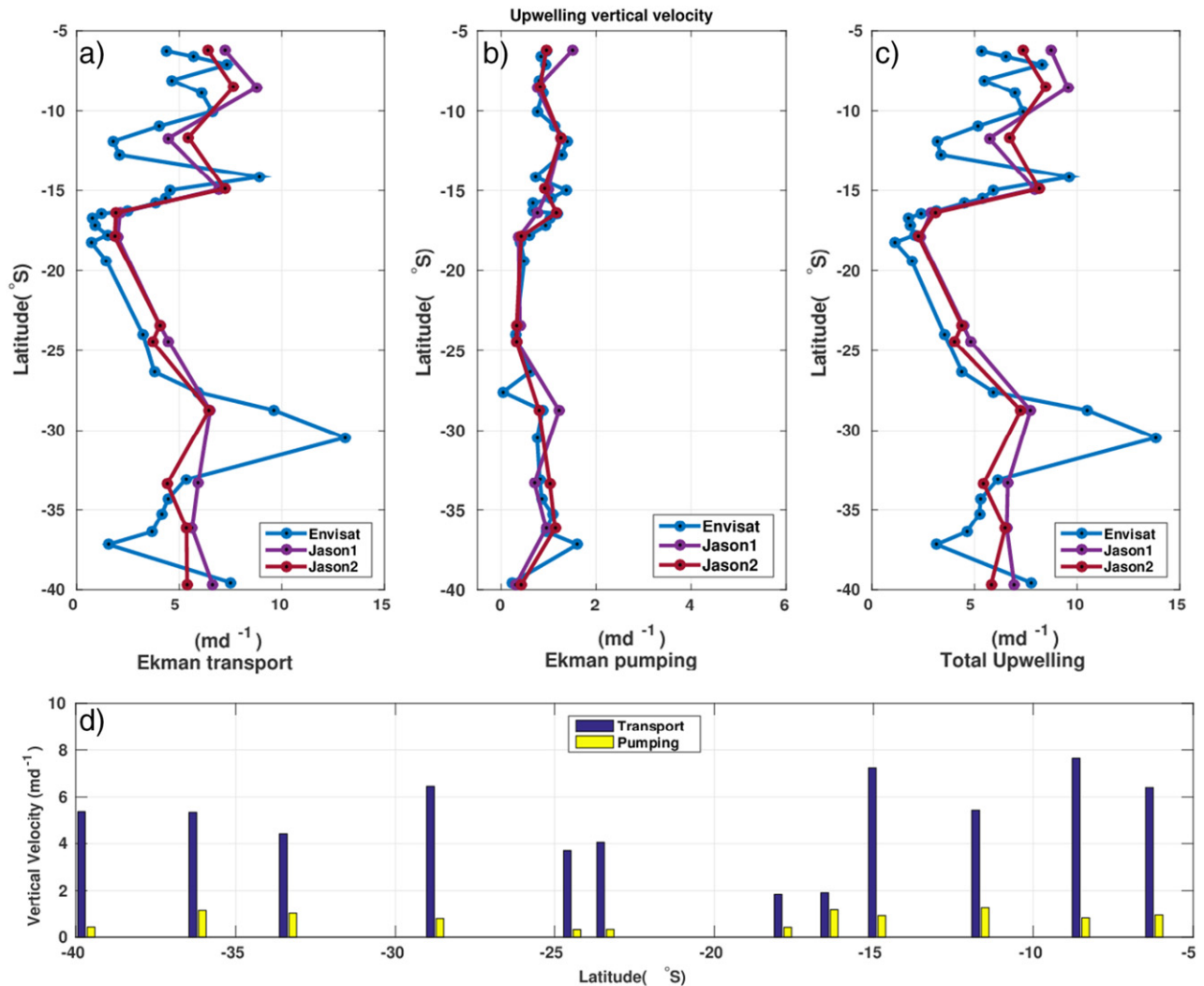
Fig. 9. Mean vertical velocities in the nearshore upwelling zone from (a) Ekman transport, (b) Ekman Pumping and (c) total upwelling (Ekman transport + Ekman pumping). (d) Comparative detail with the Jason-2 vertical velocities contributions induced by Ekman transport and Ekman pumping.

quantitatively to which extent the wind drop-off is influential on the regional oceanic circulation and biogeochemistry.

Finally, it is worth mentioning the limitations associated with the blind zone in scatterometer coverage for modeling wind-stress forcing over the inner shelf since regional ocean models are now run at high resolution spatial. Therefore special attention must be paid on how the scatterometer gridded data are extrapolated on the model grid near the coast in the region where the scatterometer data are not available. The interpolation method may indeed produce unrealistic wind stress patterns within the coastal fringe. For instance, Desbiolles et al. (2016) investigate the sensitivity of the oceanic response to the method for filling the blind zone in QuikSCAT coverage near the coast in the Benguela upwelling system using two approaches. In the first one, the estimates of surface wind stress components are extrapolated toward the coast to fill the wind data gaps in this zone, and then interpolated to the model grid. The second one completes the coastal gaps with zonal gradients derived from ECMWF reanalysis (ERA-Interim) data. The local and daily zonal gradient in the ERA-Interim meridional stress component is applied from the first missing grid cell toward the coast. They conclude that upwelling dynamics adjust quickly to a local change of the momentum fluxes, and that the upwelling circulation (i.e. surface flows and poleward undercurrent) is highly sensitive to the

alteration of the alongshore wind stress components. They show also that a wind reduction in the coastal band often reduces the SST cooling, but the two mechanisms, Ekman transport and Ekman pumping, compensate each other when the characteristic length scales of the coastal upwelling and the orography-induced wind drop-off are similar.

Altimeter data could thus provide a benchmark for evaluating the extrapolation procedure and adjust it, if necessary. Note that, at this stage, it seems difficult to go further and propose to "nudge" altimeter and scatterometer data in order to include a near-shore drop off in the scatterometer products, due to the relatively large gaps between tracks in the meridional direction.
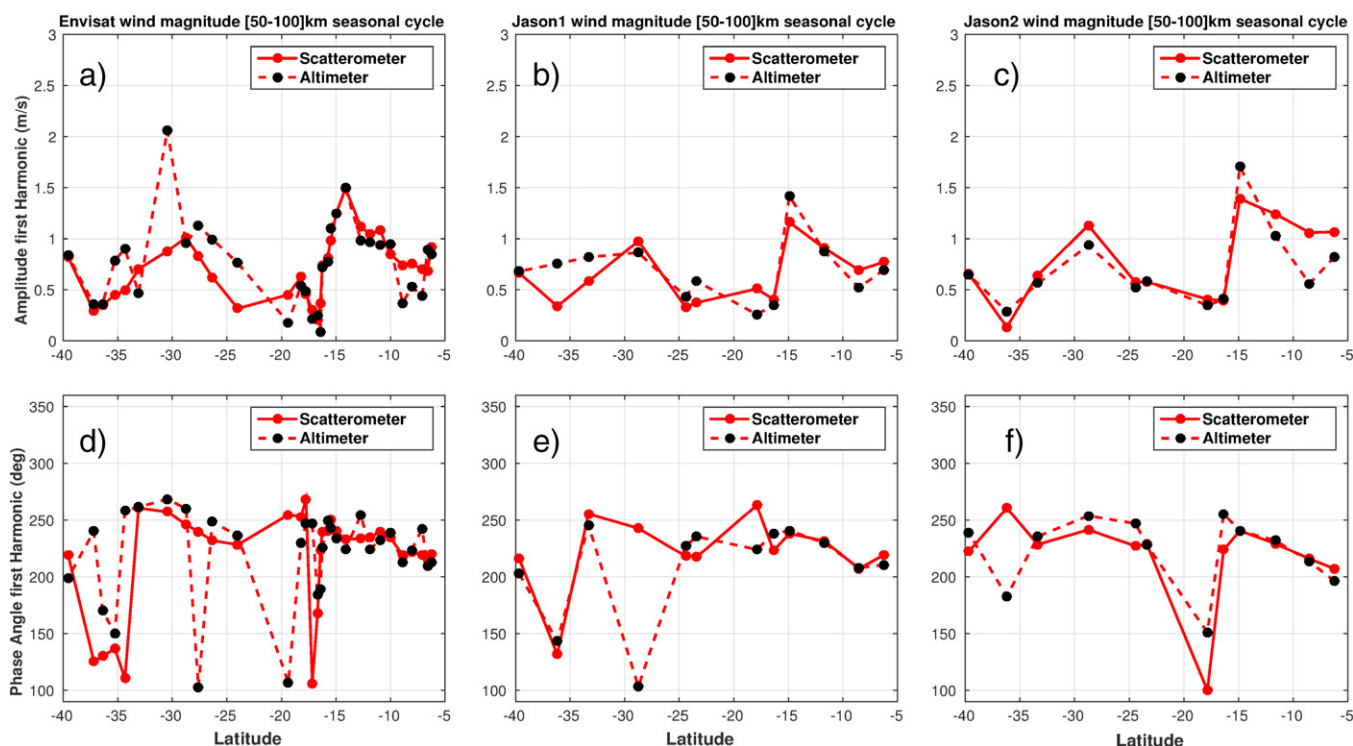
Fig. 10. Amplitude (top panels) and phase (bottom panels) of the annual harmonics of the mean wind speed near the coast (average between 50 and 100 km offshore) for the altimeter (black dots, dashed red line) and the scatterometers (red dots, plain red line). (a, d) ENVISAT, (b, e) Jason-1 and (c, f) Jason-2. (For interpretation of the references to colour in this figure legend, the reader is referred to the web version of this article.)

References

Abdalla, S., 2006. Global Validation of ENVISAT Wind, Wave and Water Vapour Products From RA-2, MWR, ASAR and MERIS, ECMWF, ESA Contract Report 17585 (81 pp).

Abdalla, S., 2012. Ku-band radar altimeter surface wind speed algorithm. Mar. Geod. 35 (Suppl. 1):276–298. http://dx.doi.org/10.1080/01490419.2012.718676 (Informa UK Limited, online).

Aguirre, C., Pizarro, Ó., Strub, P.T., Garreaud, R., Barth, J.A., 2012. Seasonal dynamics of the near-surface alongshore flow off central Chile. J. Geophys. Res. 117, C01006. http://dx.doi.org/10.1029/2011JC007379.

Albert, A., Echevin, V., Lévy, M., Aumont, O., 2010. Impact of nearshore wind stress curl on coastal circulation and primary productivity in the Peru upwelling system. J. Geophys. Res. 115 (C12). http://dx.doi.org/10.1029/2010jc006569 (Wiley-Blackwell, online).

Bakun, A., 1973. Coastal upwelling indices, west coast of North America, 1946–71. U.S. Dept. of Commerce, NOAA Tech. Rep., NMFS SSRF-671 (103p).

Bakun, A., Black, B.A., Bograd, S.J., García-Reyes, M., Miller, A.J., Rykaczewski, R.R., Sydeman, W.J., 2015. Anticipated effects of climate change on coastal upwelling ecosystems. Current Climate Change Reports 1 (2):85–93. http://dx.doi.org/10.1007/s40641-015-0008-4 (Springer Science + Business Media, online).

Bentamy, A., Fillon, D.C., 2012. Gridded surface wind fields from Metop/ASCAT measurements. Int. J. Remote Sens. 33 (6):1729–1754. http://dx.doi.org/10.1080/01431161.2011.600348 (Informa UK Limited, online).

Bentamy, A., Croize-Fillon, D., Perigaud, C., 2008. Characterization of ASCAT measurements based on buoy and QuikSCAT wind vector observations. Ocean Sci. 4 (4): 265–274. http://dx.doi.org/10.5194/os-4-265-2008 (Copernicus GmbH, online).

Blarel, F., Frappart, F., Legrésy, B., Blumstein, D., Rémy, F., Fatras, C., Mougin, E., Papa, F., Prigent, C., Niño, F., Borderies, P., Biancamaria, S., Calmant, S., 2015. Altimetry backscattering signatures at Ku and S bands over land and ice sheets. In: Neale, C.M.U., Maltese, A. (Eds.), Remote Sensing for Agriculture, Ecosystems, and Hydrology XVII, SPIE-Intl Soc Optical Eng http://dx.doi.org/10.1117/12.2194498 (online).

Bravo, L., Ramos, M., Astudillo, O., Dewitte, B., Goubanova, K., 2015. Seasonal variability of the Ekman transport and pumping in the upwelling system off central-northern Chile (~ 30° S) based on a high-resolution atmospheric regional model (WRF). Ocean Sci. Discuss. 12 (6):3003–3041. http://dx.doi.org/10.5194/osd-12-3003-2015 (Copernicus GmbH, online).

Callahan, P.S., Lungu, T. (Eds.), 2006. QuikSCAT Science Data Product User's Manual, Version 3.0. D-18053 - Rev A, JPL/NASA (85 pp).

Capet, X.J., Marchesiello, P., McWilliams, J.C., 2004. Upwelling response to coastal wind profiles. Geophys. Res. Lett. 31 (13). http://dx.doi.org/10.1029/2004gl020123 (Wiley-Blackwell, online).

Carr, M., Kearns, E.J., 2003. Production regimes in four Eastern Boundary Current systems. Deep-Sea Res. II Top. Stud. Oceanogr. 50 (22–26):3199–3221. http://dx.doi.org/10.1016/j.dsr2.2003.07.015 (Elsevier BV, online).

Chavez, F.P., Messié, M., 2009. A comparison of Eastern Boundary Upwelling Ecosystems. Prog. Oceanogr. 83 (1–4):80–96. http://dx.doi.org/10.1016/j.pocean.2009.07.032 (Elsevier BV, online).

Chavez, F.P., Bertrand, A., Guevara-Carrasco, R., Soler, P., Csirke, J., 2008, October. The northern Humboldt Current System: brief history, present status and a view towards the future. Prog. Oceanogr. http://dx.doi.org/10.1016/j.pocean.2008.10.012 (Elsevier BV).

Chelton, D.B., Walsh, E.J., MacArthur, J.L., 1989. Pulse compression and sea level tracking in satellite altimetry. J. Atmos. Ocean. Technol. 6:407–438. http://dx.doi.org/10.1175/1520-0426(1989)006,0407:PCASLT.2.0.CO;2.

Chelton, D.B., Ries, J.C., Haines, B.J., Fu, L.-L., Callahan, P.S., 2001. Chapter 1 satellite altimetry. International Geophysics. Elsevier BV http://dx.doi.org/10.1016/s0074-6142(01)80146-7 (p. 1–ii., online).

Croquette, M., Eldin, G., Grados, C., Tamayo, M., 2007. On differences in satellite wind products and their effects in estimating coastal upwelling processes in the southeast Pacific. Geophys. Res. Lett. 34 (11). http://dx.doi.org/10.1029/2006gl027538 (Wiley-Blackwell, online).

Dee, D.P., Uppala, S.M., Simmons, A.J., Berrisford, P., Poli, P., Kobayashi, S., Andrae, U., Balmaseda, M.A., Balsamo, G., Bauer, P., Bechtold, P., Beljaars, A.C.M., van de Berg, L., Bidlot, J., Bormann, N., Delsol, C., Dragani, R., Fuentes, M., Geer, A.J., Haimberger, L., Healy, S.B., Hersbach, H., Hólm, E.V., Isaksen, L., Kållberg, P., Köhler, M., Matricardi, M., McNally, A.P., Monge-Sanz, B.M., Morcrette, J.-J., Park, B.-K., Peubey, C., de Rosnay, P., Tavolato, C., Thépaut, J.-N., Vitart, F., 2011. The ERA-Interim reanalysis: configuration and performance of the data assimilation system. Q. J. R. Meteorol. Soc. 137 (656):553–597. http://dx.doi.org/10.1002/qj.828 (Wiley-Blackwell, online).

Demarcq, H., 2009. Trends in primary production, sea surface temperature and wind in upwelling systems (2000–2007). Prog. Oceanogr. 83 (1–4):376–385. http://dx.doi.org/10.1016/j.pocean.2009.07.022 (Elsevier BV, online).

Desai, S., Vincent, P., 2003, July 1. Statistical Evaluation of the Jason-1 Operational Sensor Data Record Special Issue: Jason-1 Calibration/Validation. UMGD. Informa UK Limited http://dx.doi.org/10.1080/714044518.

Desbiolles, F., Blanke, B., Bentamy, A., Roy, C., 2016. Response of the Southern Benguela upwelling system to fine-scale modifications of the coastal wind. J. Mar. Syst. 156: 46–55. http://dx.doi.org/10.1016/j.jmarsys.2015.12.002 (Elsevier BV, online).

Dewitte, B., Illig, S., Renault, L., Goubanova, K., Takahashi, K., Gushchina, D., Mosquera, K., Purca, S., 2011. Modes of covariability between sea surface temperature and wind stress intraseasonal anomalies along the coast of Peru from satellite observations (2000–2008). J. Geophys. Res. 116 (C4). http://dx.doi.org/10.1029/2010jc006495 (Wiley-Blackwell, online).

Dufois, F., Penven, P., Peter Whittle, C., Veitch, J., 2012. On the warm nearshore bias in Pathfinder monthly SST products over Eastern Boundary Upwelling Systems. Ocean Model. 47:113–118. http://dx.doi.org/10.1016/j.ocemod.2012.01.007 (Elsevier BV, online).

Figueroa, D., Moffat, C., 2000. On the influence of topography in the induction of coastal upwelling along the Chilean Coast. Geophys. Res. Lett. 27 (23):3905–3908. http://dx.doi.org/10.1029/1999gl011302 (Wiley-Blackwell, online).

Fore, A.G., Stiles, B.W., Chau, A.H., Williams, B.A., Dunbar, R.S., Rodriguez, E., 2014. Pointwise wind retrieval and ambiguity removal improvements for the QuikSCAT climatological data set. IEEE Trans. Geosci. Remote Sensing 52 (1):51–59. http://dx.doi.org/10.1109/tgrs.2012.2235843 (Institute of Electrical and Electronics Engineers (IEEE), online).

Frappart, F., Legrésy, B., Niño, F., Blarel, F., Fuller, N., Fleury, S., Birol, F., Calmant, S., 2016. An ERS-2 altimetry reprocessing compatible with ENVISAT for long-term land and ice sheets studies. Remote Sens. Environ. 184:558–581. http://dx.doi.org/10.1016/j.rse.2016.07.037 (Elsevier BV, online).

Garreaud, R., Muñoz, R.C., 2005. The low-level jet off the west coast of subtropical South America: structure and variability. Mon. Weather Rev. 133 (8):2246–2261. http://dx.doi.org/10.1175/mwr2972.1 (American Meteorological Society, online).

Garreaud, R.D., Rutllant, J.A., Muñoz, R.C., Rahn, D.A., Ramos, M., Figueroa, D., 2011. VOCALS-CUpEx: the Chilean Upwelling Experiment. Atmos. Chem. Phys. 11 (5):2015–2029. http://dx.doi.org/10.5194/acp-11-2015-2011 (Copernicus GmbH, online).

Gill, A., 1982. Atmosphere-Ocean Dynamics. Academic Press, New York.

Gourrion, J., Vandemark, D., Bailey, S., Chapron, B., Gommenginger, G.P., Challenor, P.G., Srokosz, M.A., 2002. A two-parameter wind speed algorithm for Ku-band altimeters. J. Atmos. Ocean. Technol. 19 (12):2030–2048. http://dx.doi.org/10.1175/1520-0426(2002)019<2030:atpwsa>2.0.co;2 (American Meteorological Society, online).

Halpern, D., 2002. Offshore Ekman transport and Ekman pumping off Peru during the 1997–1998 El Niño. Geophys. Res. Lett. 29 (5):19-1–19-4. http://dx.doi.org/10.1029/2001gl014097 (Wiley-Blackwell, online).

Hill, A.E., Hickey, B., Shillington, F., Strub, P.T., Brink, K.H., Barton, E., Thomas, A., 1998. Eastern boundary currents: a pan-regional review. In: Robinson, A.R., Brink, K.H. (Eds.), The SeaThe Global Coastal Ocean: Regional Studies and Syntheses vol. 11. John Wiley, Hoboken, N. J, pp. 29–68.

Ikeda, M., Dobson, F., 1995. Oceanographic Applications of Remote Sensing. CRC Press, Boca Raton.

KNMI, 2010. Metop-A ASCAT Level 2 Ocean Surface Wind Vectors Optimized for Coastal Ocean. Ver. Operational/Near-real-time. PO.DAAC, CA, USA (Dataset accessed [2014-06-01]).

KNMI, 2013. Metop-B ASCAT Level 2 Ocean Surface Wind Vectors Optimized for Coastal Ocean. Ver. Operational/Near-Real-Time. PO.DAAC, CA, USA (Dataset accessed [2014-06-01]).

Large, W., Pond, S., 1981. Open ocean momentum flux measurements in moderate to strong winds. J. Phys. Oceanogr. 11, 324–336.

Lefèvre, J.M., Aouf, L., Skandrani, S., Queffeulou, P., 2006. Contribution of satellite altimetry to wave analysis and forecasting. 15 Years of Progress in Radar Altimetry Symposium, Venice, Italy.

Lillibridge, J., Scharroo, R., Abdalla, S., Vandemark, D., 2014. One- and two-dimensional wind speed models for Ka-band altimetry. J. Atmos. Ocean. Technol. 31 (3):630–638. http://dx.doi.org/10.1175/jtech-d-13-00167.1 (American Meteorological Society, online).

Lin, J.W.-B., Neelin, J.D., Zeng, N., 2000. Maintenance of tropical intraseasonal variability: impact of evaporation–wind feedback and midlatitude storms. J. Atmos. Sci. American Meteorological Society http://dx.doi.org/10.1175/1520-0469(2000)057<2793:motivi>2.0.co;2.

Machu, E., Ettahiri, O., Kifani, S., Benazzouz, A., Makaoui, A., Demarcq, H., 2009. Environmental control of the recruitment of sardines (Sardina pilchardus) over the western Saharan shelf between 1995 and 2002: a coupled physical/biogeochemical modelling experiment. Fish. Oceanogr. 18 (5):287–300. http://dx.doi.org/10.1111/j.1365-2419.2009.00511.x (Wiley-Blackwell, online).

Marchesiello, P., Estrade, P., 2010, January 1. Upwelling limitation by onshore geostrophic flow. J. Mar. Res. http://dx.doi.org/10.1357/002224010793079004.

Messié, M., Ledesma, J., Kolber, D.D., Michisaki, R.P., Foley, D.G., Chavez, F.P., 2009. Potential new production estimates in four eastern boundary upwelling ecosystems. Prog. Oceanogr. 83 (1–4):151–158. http://dx.doi.org/10.1016/j.pocean.2009.07.018 (Elsevier BV, online).

Monaldo, F., 1988. Expected differences between buoy and radar altimeter estimates of wind speed and significant wave height and their implications on buoy-altimeter comparisons. J. Geophys. Res. http://dx.doi.org/10.1029/jc093ic03p02285 (Wiley-Blackwell).

Muñoz, R.C., 2008. Diurnal cycle of surface winds over the subtropical southeast Pacific. J. Geophys. Res. 113 (D13). http://dx.doi.org/10.1029/2008jd009957 (Wiley-Blackwell, online).

Penven, P., 2005. Average circulation, seasonal cycle, and mesoscale dynamics of the Peru Current System: a modeling approach. J. Geophys. Res. http://dx.doi.org/10.1029/2005jc002945 (Wiley-Blackwell, online).

Penven, P., Roy, C., Brundrit, G., Colin de Verdière, A., Fréon, P., Johnson, A., Lutjeharms, J., Shillington, F., 2001. A regional hydrodynamic model of upwelling in the Southern Benguela. S. Afr. J. Sci. 97 (11–12), 472–475.

Pickett, M.H., Paduan, J.D., 2003. Ekman transport and pumping in the California Current based on the U.S. Navy's high-resolution atmospheric model (COAMPS). J. Geophys. Res. 108 (C10):3327. http://dx.doi.org/10.1029/2003JC001902 (Wiley-Blackwell).

Queffeulou, P., 2003. Validation of ENVISAT RA-2 and JASON-1 altimeter wind and wave measurements. IGARSS 2003. 2003 IEEE International Geoscience and Remote Sensing Symposium. Proceedings (IEEE Cat. No. 03CH37477). Institute of Electrical & Electronics Engineers (IEEE) http://dx.doi.org/10.1109/igarss.2003.1294656 (online).

Queffeulou, P., Chapron, B., Bentamy, A., 1999. Comparing Ku-band NSCAT scatterometer and ERS-2 altimeter winds. IEEE Trans. Geosci. Remote Sensing 37 (3):1662–1670.

http://dx.doi.org/10.1109/36.763285 (Institute of Electrical & Electronics Engineers (IEEE), online).

Quilfen, Y., Prigent, C., Chapron, B., Mouche, A.A., Houti, N., 2007, September 27. The potential of QuikSCAT and WindSat observations for the estimation of sea surface wind vector under severe weather conditions. J. Geophys. Res. http://dx.doi.org/10.1029/2007jc004163 (Wiley-Blackwell).

Rahn, D.A., 2012. Influence of large scale oscillations on upwelling-favorable coastal wind off central Chile. J. Geophys. Res. Atmos. http://dx.doi.org/10.1029/2012jd018016 (Wiley-Blackwell).

Rahn, D.A., Garreaud, R.D., 2013. A synoptic climatology of the near-surface wind along the west coast of South America. Int. J. Climatol. 34 (3):780–792. http://dx.doi.org/10.1002/joc.3724 (Wiley-Blackwell, online).

Ray, R.D., Beckley, B.D., 2003. Simultaneous Ocean Wave Measurements by the Jason and Topex Satellites, with Buoy and Model Comparisons Special Issue: Jason-1 Calibration/Validation. UMGD. Informa UK Limited http://dx.doi.org/10.1080/714044527.

Renault, L., Dewitte, B., Falvey, M., Garreaud, R., Echevin, V., Bonjean, F., 2009. Impact of atmospheric coastal jet off central Chile on sea surface temperature from satellite observations (2000–2007). J. Geophys. Res. 114 (C8). http://dx.doi.org/10.1029/2008jc005083 (Wiley-Blackwell, online).

Renault, L., Dewitte, B., Marchesiello, P., Illig, S., Echevin, V., Cambon, G., Ramos, M., Astudillo, O., Minnis, P., Ayers, J.K., 2012. Upwelling response to atmospheric coastal jets off central Chile: a modeling study of the October 2000 event. J. Geophys. Res. 117 (C2). http://dx.doi.org/10.1029/2011jc007446 (Wiley-Blackwell, online).

Renault, L., Deutsch, C., McWilliams, J.C., Frenzel, H., Liang, J.H., Colas, F., 2016. Partial decoupling of primary productivity from upwelling in the California Current system. Nat. Geosci. 9 (7):505–508. http://dx.doi.org/10.1038/ngeo2722 (Springer Nature).

Renault, L., Hall, A., McWilliams, J.C., 2015. Orographic shaping of US West Coast wind profiles during the upwelling season. Clim. Dyn. http://dx.doi.org/10.1007/s00382-015-2583-4 (Springer Science + Business Media).

Rutllant, J.A., Rosenbluth, B., Hormazabal, S., 2004, May. Intraseasonal variability of wind-forced coastal upwelling off central Chile (30°S). Cont. Shelf Res. http://dx.doi.org/10.1016/j.csr.2004.02.004 (Elsevier BV).

Saha, S., Moorthi, S., Pan, H.-L., Wu, X., Wang, J., Nadiga, S., Tripp, P., Kistler, R., Woollen, J., Behringer, D., Liu, H., Stokes, D., Grumbine, R., Gayno, G., Wang, J., Hou, Y.-T., Chuang, H.-Y., Juang, H.-M.H., Sela, J., Iredell, M., Treadon, R., Kleist, D., Van Delst, P., Keyser, D., Derber, J., Ek, M., Meng, J., Wei, H., Yang, R., Lord, S., Van Den Dool, H., Kumar, A., Wang, W., Long, C., Chelliah, M., Xue, Y., Huang, B., Schemm, J.-K., Ebisuzaki, W., Lin, R., Xie, P., Chen, M., Zhou, S., Higgins, W., Zou, C.-Z., Liu, Q., Chen, Y., Han, Y., Cucurull, L., Reynolds, R.W., Rutledge, G., Goldberg, M., 2010. The NCEP climate forecast system reanalysis. Bull. Am. Meteorol. Soc. 91 (8):1015–1057. http://dx.doi.org/10.1175/2010bams3001.1 (American Meteorological Society, online).

SeaPAC, 2013. QuikSCAT Level 2B Ocean Wind Vectors in 12.5km Slice Composites Version 3. Ver. 3. PO.DAAC, CA, USA http://dx.doi.org/10.5067/QSX12-L2B01 (Dataset accessed [2014-06-01]).

Shanas, P.R., Sanil Kumar, V., Hithin, N.K., 2014, June. Comparison of gridded multi-mission and along-track mono-mission satellite altimetry wave heights with in situ near-shore buoy data. Ocean Eng. http://dx.doi.org/10.1016/j.oceaneng.2014.03.014 (Elsevier BV).

Silva, A., Palma, S., Oliveira, P.B., Moita, M.T., 2009. Composition and interannual variability of phytoplankton in a coastal upwelling region (Lisbon Bay, Portugal). J. Sea Res. 62 (4):238–249. http://dx.doi.org/10.1016/j.seares.2009.05.001 (Elsevier BV, online).

Smith, R.L., 1968. Upwelling. Oceanogr. Mar. Biol. Annu. Rev. 6, 11–46.

Sverdrup, H.U., Johnson, M.W., Fleming, R.H., 1942. The Oceans, Their Physics, Chemistry, and General Biology. Prentice-Hall Inc.

Tierney, C., Wahr, J., Bryan, F., Zlotnicki, V., 2000. Short-period oceanic circulation: Implications for satellite altimetry. Geophys. Res. Lett. 27 (9):1255–1258. http://dx.doi.org/10.1029/1999gl010507 (Wiley-Blackwell, online).

Veitch, J., Penven, P., Shillington, F., 2009. The Benguela: a laboratory for comparative modeling studies. Prog. Oceanogr. 83 (1–4):296–302. http://dx.doi.org/10.1016/j.pocean.2009.07.008 (Elsevier BV, online).

Verhoef, A., Stoffelen, A., 2013. Validation of ASCAT Coastal Winds, Version 1.5 Document External Project: 2013, SAF/OSI/CDOP/KNMI/TEC/RP/176, EUMETSAT.

Verron, J., Sengenes, P., Lambin, J., Noubel, J., Steunou, N., Guillot, A., Picot, N., Coutin-Faye, S., Sharma, R., Gairola, R.M., Murthy, D.V.A.R., Richman, J.G., Griffin, D., Pascual, A., Rémy, F., Gupta, P.K., 2015. The SARAL/AltiKa altimetry satellite mission. Mar. Geod. 38 (Suppl. 1):2–21. http://dx.doi.org/10.1080/01490419.2014.1000471 (Informa UK Limited, online).

Vogelzang, J., Stoffelen, A., Verhoef, A., Figa-Saldaña, J., 2011, October 28. On the quality of high-resolution scatterometer winds. J. Geophys. Res. http://dx.doi.org/10.1029/2010jc006640 (Wiley-Blackwell).

Wang, Q., Kalogiros, J., Ramp, S., Paduan, J., Buzorius, G., Jonsson, H., 2011. Wind stress curl and coastal upwelling in the area of Monterey Bay observed during AOSN-II. J. Phys. Oceanogr. 41 (5), 857–877.

Wang, Y., Castelao, R.M., Yuan, Y., 2015a. Seasonal variability of alongshore winds and sea surface temperature fronts in Eastern Boundary Current Systems. J. Geophys. Res. Oceans 120 (3):2385–2400. http://dx.doi.org/10.1002/2014jc010379 (Wiley-Blackwell, online).

Wang, D., Gouhier, T.C., Menge, B.A., Ganguly, A.R., 2015b. Intensification and spatial homogenization of coastal upwelling under climate change. Nature 518 (7539):390–394. http://dx.doi.org/10.1038/nature14235 (Nature Publishing Group, online).

Wood, R., Mechoso, C.R., Bretherton, C.S., Weller, R.A., Huebert, B., Straneo, F., Albrecht, B.A., Coe, H., Allen, G., Vaughan, G., Daum, P., Fairall, C., Chand, D., Gallardo Klenner, L., Garreaud, R., Grados, C., Covert, D.S., Bates, T.S., Krejci, R., Russell, L.M., de Szoeke, S., Brewer, A., Yuter, S.E., Springston, S.R., Chaigneau, A., Toniazzo, T., Minnis, P.,

Palikonda, R., Abel, S.J., Brown, W.O.J., Williams, S., Fochesatto, J., Brioude, J., Bower, K.N., 2011. The VAMOS Ocean-Cloud-Atmosphere-Land Study Regional Experiment (VOCALS-REx): goals, platforms, and field operations. Atmos. Chem. Phys. 11 (2): 627–654. http://dx.doi.org/10.5194/acp-11-627-2011 (Copernicus GmbH, online).

Yang, X., Li, X., Pichel, W.G., Li, Z., 2011. Comparison of ocean surface winds from ENVISAT ASAR, Metop ASCAT scatterometer, buoy measurements, and NOGAPS model. IEEE Trans. Geosci. Remote Sensing 49 (12):4743–4750. http://dx.doi. org/10.1109/tgrs.2011.2159802 (Institute of Electrical & Electronics Engineers (IEEE), online).

Zieger, S., Vinoth, J., Young, I.R., 2009. Joint calibration of multiplatform altimeter measurements of wind speed and wave height over the past 20 years. J. Atmos. Ocean. Technol. 26 (12):2549–2564. http://dx.doi.org/10.1175/2009jtecha1303.1 (American Meteorological Society, online).